# Deciphering the evolution of the Bleis Marscha rock glacier (Val d'Err, eastern Switzerland) with cosmogenic nuclide exposure dating, aerial image correlation, and finite element modelling

Dominik Amschwand[1,3], Susan Ivy-Ochs[1,2], Marcel Frehner[1], Olivia Steinemann[2], Marcus Christl[2], Christof Vockenhuber[2]

[1]Department of Earth Sciences, ETH Zurich, 8092, Zurich, Switzerland
[2]Laboratory of Ion Beam Physics, ETH Zurich, 8093, Zurich, Switzerland
[3]Now at: Department of Geosciences, University of Fribourg, 1700, Fribourg, Switzerland

*Correspondence to*: Dominik Amschwand (dominik.amschwand@unifr.ch) ORCID: 0000-0003-2179-1481

**Abstract.** We constrain the Holocene development of the active Bleis Marscha rock glacier (Err-Julier area, eastern Swiss Alps) with 15 cosmogenic nuclide exposure ages ($^{10}$Be, $^{36}$Cl), horizontal surface creep rate quantification by correlating two orthophotos from 2003 and 2012, and finite element modelling to separate the control exerted by topography and material composition on surface movement. Bleis Marscha is a stack of three overriding lobes whose formation phases are separated by 'time gaps' expressed morphologically as over-steepened terrain steps and kinematically as sharp downslope decrease in surface movement. The three discrete formation phases appear to be correlated to major Holocene climate shifts: Early Holocene low-elevation lobes (~8.9–8.0 ka, after Younger Dryas), Middle Holocene lobe (~5.2–4.8 ka, after thermal maximum), and Late Holocene high-elevation lobes (active since ~2.8 ka, coexisting with intermittent Bleis Marscha cirque glacierets). The formation phases appear to be controlled in the source area by the climate sensitive accumulation of an ice-debris mixture in proportions necessary for rock glaciers and susceptible to creep. Ongoing cohesive movement of the older generations requires ice at depth which is possibly as old as its early-/mid-Holocene debris mantle. Permafrost degradation is attenuated by 'thermal filtering' of the coarse debris boulder mantle, and implies that the dynamics of the Bleis Marscha lobes, that persisted over millennia once formed, are less sensitive to climate. The cosmogenic radionuclide inventories of boulders on a moving rock glacier ideally record time since deposition on the rock glacier root, but are stochastically altered by boulder instabilities and erosional processes. This work contributes to deciphering the long-term development and the past to quasi-present climate sensitivity of rock glaciers.

## 1 Introduction

Active rock glaciers are defined as "lobate or tongue-shaped bodies of perennially frozen unconsolidated material supersaturated with interstitial ice and ice lenses that move downslope or downvalley by creep as a consequence of the deformation of ice contained in them and which are, thus, features of cohesive flow" (Barsch, 1996). Their active phase and

30 development are conditioned by ice preservation, permafrost conditions (Haeberli et al., 2006), and debris supply (Kenner and Magnusson, 2017).

In our current warming climate (Hock et al., 2019), active rock glaciers as the "visible expression of mountain permafrost" (Barsch, 1996) receive considerable attention. Their surface kinematics is considered as diagnostic for the thermal state of mountain permafrost (Delaloye et al., 2018), which is otherwise not directly observable. Rock glaciers are thought to store

35 significant water resources (Jones et al., 2019) and become more significant in the deglaciating mountains (Haeberli et al., 2017; Knight et al., 2019). However, in the literature, different views on the climate sensitivity of rock glaciers are proposed. One concept is that rock glaciers respond attenuated and delayed to current warming because of the high thermal inertia of the ice-rich core and the thermal decoupling from external climate by the insulating effect of the boulder mantle (active layer) (e.g. Haeberli et al., 2017; Anderson et al., 2018) via the 'thermal semi-conductor' effect (Harris and Pedersen, 1998;

40 Humlum, 1998; Hanson and Hoelzle, 2004). The ground cooling effect of a coarse debris mantle (Schneider et al., 2012; Wicky and Hauck, 2017) favours a large negative thermal offset and permafrost conditions even at mean annual ground temperature (MAGT) close to 0 °C (Kellerer-Pirklbauer, 2019). Furthermore, the creep of millennia-old rock glaciers is tied to the ice-supersaturation of the debris and hence to the preservation of ice over their entire lifetime (Barsch, 1996; Haeberli et al., 2003). Another concept is the synchronous, rapid response to warming, based on kinematic rock glacier monitoring.

45 Many rock glaciers across the Alps show a common behaviour of surface creep rates with (sub)seasonal fluctuations (Delaloye et al., 2010). These decennial to annual changes in surface creep rates respond within months to changing summer air temperature and snow cover timing (Noetzli et al., 2019). Rock glacier formation can occur within centuries (Humlum, 1996), or under very specific topo-climatic conditions even within decades (Scotti et al., 2017). Debris pulses or "surge packages" (Kenner et al., 2014), as well as "significant acceleration", destabilization (Marcer et al., 2019) up to "sudden

50 collapse" (Bodin et al., 2016) are reported.

The response of rock glaciers to external forcings such as air temperature, precipitation and snow cover, weathering intensity, debris supply, and interactions with glaciers (e.g. pushing ice, altered thermal conditions/insulation, glacial debris sources) are insufficiently understood. Furthermore, their external response is difficult to disentangle from internal thermo-mechanical and topographic feedbacks. Historical records are too short compared to typical rock glacier lifetimes, activity

55 phases and response periods. To resolve long-term effects on rock glacier development (Kenner and Magnusson, 2017) and to put the present-day morphology reflecting the lifelong dynamic history of active rock glaciers and (relict) rock glacier deposits in a climate sensitivity context (Frauenfelder and Kääb, 2000), their activity phases need to be placed in a chronological framework. Cosmogenic radionuclide concentrations record all periods of exposure of the rock surface to cosmic rays. In principle, they are a suitable tool for deriving numerical exposure ages for boulders on the landform surface

60 (Ivy-Ochs and Kober, 2008). The technique has been applied on (relict) rock glaciers deposits or related periglacial landforms by Ivy-Ochs et al. (2009), Böhlert (2011a, b), Moran et al. (2016), Denn et al. (2017, and references therein), and

Steinemann et al. (2020). Relict and active rock glacier deposits in Iceland were exposure dated by Férnandez-Férnandez et al. (2020).

In this study, our focus is on the Bleis Marscha rock glacier located in the Err-Julier area, eastern Swiss Alps (Fig. 1). Previous relative dating studies based on Schmidt-hammer rebound values as well as thickness and chemical composition of weathering rinds suggest a Holocene-long development (Frauenfelder et al., 2001; 2005; Laustela et al., 2003). We exposure date 15 boulders along a longitudinal transect from the lowermost front up to the transition towards the talus with the cosmogenic radionuclides $^{10}$Be and $^{36}$Cl. This is the first study that exposure dates boulders on an active, presently moving rock glacier lobe in the Alps. The exposure ages are interpreted in light of field observations, modern surface creep quantification through image correlation, and numerical finite element (FE) modelling to unveil periods of activity and the development of the Bleis Marscha rock glacier. This work contributes to deciphering the past to quasi-present climate sensitivity of rock glaciers in a high-mountain environment.

## 2 Study site

The studied Bleis Marscha rock glacier (WGS 84: 46°34′18″N, 9°42′12″E; CH1903+ / LV95: 2'773'595, 1'160'326) lies on the eastern slope of the upper Val d'Err, a side valley of the Surses (Oberhalbstein) in the Err-Julier area, Grisons, eastern Swiss Alps (Fig. 1). The rock glacier originates in a NNW-oriented cirque of Piz Bleis Marscha (3127 m a.s.l.).

The Err-Julier area lies in the rain shadow of the Lepontine, Bernese and Glarus Alps resulting in a dry-cold, continental-type climate. Frauenfelder et al. (2001) report low mean annual precipitation (MAP) of 900–1000 mm a$^{-1}$ (1971–1990), a regional lapse rate of 0.55°C/100 m and a mean annual 0 °C-isotherm at c. 2180 m a.s.l. Val d'Err is a high valley with the valley floor at an elevation above 2000 m a.s.l. and surrounding peaks rising to over 3000 m a.s.l. The present-day lower limit of permafrost occurrence is roughly at 2400 m a.s.l. (Gruber et al., 2006; Boeckli et al., 2012).

The north-northwest to south-southeast oriented valley lies in a tectonically complex zone between the Upper Penninic Platta nappe overlain by the Lower Austroalpine Err nappe. The debris-supplying headwalls (in Tschirpen unit of the Err nappe) are composed of post-Variscan granitoids and Permo-Triassic to Lower Cretaceous sediments (mostly slate and carbonates), separated by a thrust outcropping subhorizontally along the cirque walls (Cornelius, 1932; Frauenfelder et al., 2005).

During the Last Glacial Maximum (LGM) around 24 ka (Ivy-Ochs, 2015), the area was covered up to an elevation of ~2800 m a.s.l. by ice flowing northwards from the nearby Engadine ice dome (Inn River catchment) into the Rhine glacier system (Bini et al., 2009). Prominent presumed Lateglacial (Egesen) moraines along the valley flanks (Schlosser, 1990; Frauenfelder et al., 2001) suggest that the upper Val d'Err, including our study site, was likely last occupied by a glacier during the Egesen stadial (12.9–11.7 ka (Ivy-Ochs, 2015)). The Bleis Marscha cirque was occupied by a glacieret during the Little Ice Age (LIA) and up until recently (Dufour, 1853; Frauenfelder et al., 2001).
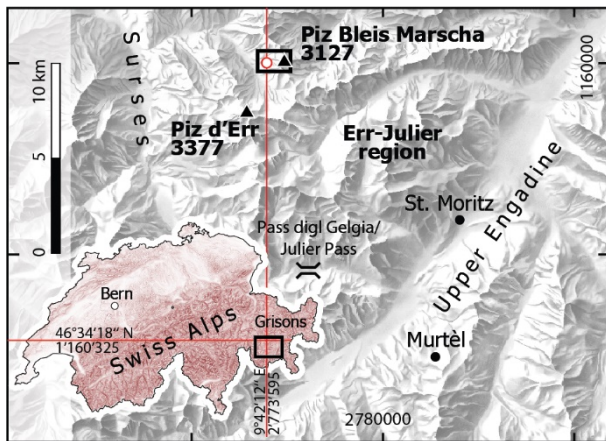
**Figure 1: Location of the Bleis Marscha rock glacier to the west below Piz Bleis Marscha in the Err-Julier region, eastern Swiss Alps. The rectangle shows the area covered by the geomorphological map (Fig. 3). Inset map: Location and extent (black**
95 **rectangle) of the Err-Julier regional map within Switzerland and the coordinates of the lowermost front of the Bleis Marscha rock glacier (Maps reproduced with the authorization of the Swiss Federal Office of Topography swisstopo).**

## 3 Material and Methods

Topographic maps, aerial photographs, digital elevation models, geomorphological field mapping, surface exposure dating, and finite element (FE) modelling form the data basis to reconstruct the Bleis Marscha development. The morphology of
100 rock glaciers, where processes and form are intrinsically linked via deformation by creep, largely preserves the cumulative deformation history over the lifetime of the landform (cf. Frauenfelder and Kääb, 2000). The concept of rock glacier formation and the 'conveyor belt'-like advance mechanism form the theoretical groundwork on how surface boulders move compared to the rock glacier as a whole (outlined in Sects. 5.1–5.2). The subdivision in geomorphologically defined units of the polymorphic (sensu Frauenfelder and Kääb, 2000) Bleis Marscha rock glacier, assisted by an estimate of modern surface
105 creep rates from aerial image correlation, provides a framework for the discussion and interpretation of the exposure ages. Surface exposure ages of 15 boulders of the rock glacier deposit were determined with the cosmogenic radionuclides $^{10}$Be and $^{36}$Cl. FE modelling separates the control of topography and material properties (e.g. ice content at depth) to the surface creep rate pattern.

### 3.1 Field work and Bleis Marscha landform analysis

110 Field mapping was performed in August 2017, focusing on Quaternary geology and geomorphology. Fieldwork was carried out at the scale of 1:5000 following standard geomorphological mapping procedures as outlined in Chandler et al. (2018). Details of the landforms and sediment of various sectors of the rock glacier were characterized to, in concert with digital elevation model (DEM) analysis, subdivide it into different lobes. Especially distinguishing were lichen coverage (leading to

pale vs. dark appearance of the blocks) and general freshness of the blocks, the location of ridges and furrows and the presence of steep steps in the rock glacier, as well as dominant size and rounding of blocks. Crosscutting relationships with talus and rockfall deposits, moraines and the past location of the cirque glacier were also examined based on historical maps. Landform interpretation was supported by aerial and DEM data in the iPad with Garafa GIS Pro application accessed in the field. Photos taken in the field and locations of boulders sampled for cosmogenic nuclide exposure dating were thus automatically georeferenced. Orthorectified aerial images (0.25×0.25 m resolution) and the high-resolution DEM "swissALTI3D" provided by the Swiss Federal Office of Topography (swisstopo) served for topographic analysis and visualization. The DEM, acquired in 2016, is gridded on 2×2 m cells (resolution) and has an average error of ± 1–3 m (1σ level accuracy) for areas above 2000 m a.s.l. Extraction of swath profiles and morphometric calculations were carried out with the Matlab toolbox TopoToolbox 2 (Schwanghart and Scherler, 2014) and the open-source software QGIS.

### 3.2 $^{10}$Be and $^{36}$Cl exposure dating

Suitable boulders are large (>1.5 m side length) and in a stable position; suitable rock surfaces do not show signs of fast weathering or spalling. 15 boulders on the rock glacier surface suitable for exposure dating were sampled with hammer, chisel, and battery-powered saw according to guidelines of Ivy-Ochs and Kober (2008) and field observations. Topographic shielding, dip, and dip direction of sampled surfaces were measured using a compass and clinometer. The samples (~0.5 kg of rock material each) were collected close to the central flow line from the lowermost front up to the high-elevation active lobes, preferentially on ridges to minimise topographic and snow shielding (Böhlert et al., 2011b) and towards the frontal upper edge of each morphologically identified lobe (Haeberli et al., 2003; Steinemann et al., 2020). 14 samples were Julier granodiorite (quartz, $^{10}$Be; Table 1); only one dolomite boulder for $^{36}$Cl met the sampling criteria (Table 2).

$^{10}$Be sample preparation followed Kronig et al. (2018). The ratio of $^{10}$Be/$^{9}$Be is measured with the 600 kV Tandy at the ETH Zürich Accelerator Mass Spectrometry (AMS) facility (Christl et al., 2013). The in-house standard S2007N, which is calibrated against the 07KNSTD was used. For $^{36}$Cl extraction from the dolomite sample (Err8), the method of isotope dilution was employed (Ivy-Ochs et al., 2004). Concentrations of major and trace elements were measured by ICP-MS (Inductively Coupled Plasma Mass Spectrometry) at Actlabs (Ontario, Canada) (Table 3). AMS measurements were conducted with the 6 MV Tandem accelerator (Synal et al., 1997; Vockenhuber et al., 2019) of the Laboratory of Ion Beam Physics, ETH Zurich.

The $^{10}$Be surface exposure ages were calculated from the blank-corrected data (long-time laboratory blank of $^{10}$Be/$^{9}$Be = (3.2 ± 1.4) × $10^{-15}$) using the CRONUS-EARTH online calculator (Balco et al. 2008) with the North-eastern North America (NENA) $^{10}$Be production rate of 3.87 ± 0.19 atoms $g^{-1}$ $a^{-1}$ and the scaling model by Lal (1991)/Stone (2000). The shielding parameters were calculated with the "online calculators formerly known as the CRONUS-Earth online calculators" (Balco et al., 2008, http://hess.ess.washington.edu/math). The NENA production rate has been shown to be well applicable for the Alpine area (Claude et al., 2014). The $^{36}$Cl surface exposure age was computed with an ETH Laboratory of Ion Beam

Physics (LIP) in-house developed MATLAB program based on the equations and constants given in Alfimov and Ivy-Ochs (2009, and references therein). $^{36}$Cl production in dolomite is dominated by spallation of Ca, muon interactions with Ca and low-energy neutron capture reflecting the high natural Cl concentration (Err8: 49.6 ± 0.1 ppm, Table 2). The following production rates were used: 48.8 ± 3.4 $^{36}$Cl atoms g$^{-1}$ a$^{-1}$ for spallation in Ca and 5.3 ± 1.0 $^{36}$Cl atoms g$^{-1}$ a$^{-1}$ for muon capture

150   in Ca at the rock surface. A neutron capture rate of 760 ± 150 neutrons/g$_{air}$ (Alfimov and Ivy-Ochs, 2009) was implemented. We used the Lal/Stone scaling of the production rates to the site latitude, longitude, and elevation (Balco et al., 2008).

We report and discuss exposure ages with an erosion rate of 1 mm kyr$^{-1}$ for the crystalline samples ($^{10}$Be) and 5 mm kyr$^{-1}$ for the dolomite sample ($^{36}$Cl). Snow-cover corrections are omitted as such corrections would increase the exposure ages by only a few percent (by 6% for 50 cm of snow during 6 months a year). The reported errors are at the 1σ level including

155   analytical uncertainties of the AMS measurements and the blank correction (internal errors).

### 3.3 Estimation of modern surface creep rates

We quantify the horizontal surface creep rate with the cross-correlation of orientation images (Fitch et al., 2002) derived from two ortho-images with the Matlab tool ImGRAFT (Messerli and Grinsted, 2015).The orthophoto mosaic *swissimage 25 cm* is a composite of orthorectified digital color aerial photographs, provided by the Swiss Federal Office of Topography

160   (swisstopo). Ground resolution is given as 0.25 m, positional accuracy as ± 0.25 m.

The orientation correlation method developed by Fitch et al. (2012) is a feature-based method of translatory image matching that matches the orientation of the image intensity gradients. Orientation images are normalized and invariant to pixel brightness, making the method more robust and less susceptible to different illumination in the images. We derived the orientation images from the R band of the RGB images.

165   The post-processing steps are noise filtering to remove erroneous matches and smoothing to attenuate small-scale and thus likely short-lived creep-rate variations. A minimum correlation coefficient of 0.6 and a conservative signal-to-noise ratio threshold of 6 sufficed to remove incoherent and poor-quality displacement vectors. The optimal template size of 51×51 pixels was found using a procedure after Debella-Gilo and Kääb (2012). The search windows size of 211×211 pixels was defined with the recommendations of Messerli and Grinsted (2015). The modal displacement of the presumably stable

170   adjacent off-rock glacier areas defined the significance level, that is the threshold below which any measured displacement is not distinguishable from immobility.

### 3.4 Finite element modelling

The surface movement of a rock glacier integrates the overall vertical deformation profile (Müller et al., 2016). An appropriate flow law – a mathematical formulation of the governing deformation process – allows in principle to infer from

175    (known, observable) surface properties to (unknown) effective material properties and structures at depth that cause the observed deformation.

The first-order deformation of rock glaciers is governed by gravity-driven steady-state creep of its ice-bonded interior (Müller et al., 2016). In case of ice-supersaturation, the deformable (excess) ice leads to stress transfer in space and time and therefore to a cohesive surface creep rate pattern, a diagnostic feature of active rock glaciers. Creep of permafrost can be

180    approximately described by Glen's flow law for polycrystalline ice (Haeberli et al, 2006), establishing a constitutive power-law relationship between shear stresses $\tau$ [Pa] and shear strain rates $\dot{\varepsilon}$ [s$^{-1}$]. The surface speed $u_s$ [m s$^{-1}$] of an infinite, parallel-sided slab using Glen's flow law is

$$u_s = \frac{2A}{n+1} (\rho g \sin \bar{\alpha})^n H^{n+1}, \tag{1}$$

with flow rate factor $A$ [Pa$^{-n}$ s$^{-1}$] related to dynamic viscosity $\mu := \frac{\tau}{2\dot{\varepsilon}} = (2A\tau^{n-1})^{-1}$ [Pa s], stress exponent $n$ [-], density $\rho$

185    [kg m$^{-3}$], average surface slope $\bar{\alpha}$ [°], thickness $H$ [m], and gravitational acceleration $g$ [9.81 m s$^{-2}$]. However, Eq. (1) is underdetermined, and no unique solution exists. A simultaneous determination of material properties (density, viscosity) and structure (thickness) is not possible. This inverse problem requires regularization to become solvable, i.e. all but one of these parameters need to be estimated independently.

The rock glacier model is mechanically described by the model parameters $H$, $\bar{\alpha}$, $\rho$, and $\mu$. We invert for effective dynamic

190    viscosity $\mu$, from known surface slope $\bar{\alpha}$, and surface speed data $u_s$. We regularise the inverse problem by a-priori prescribing density $\rho$, and thickness $H$, parameters that can be reasonably well estimated from literature knowledge and field observations (Fig. 2a). In absence of any Bleis Marscha rheological borehole data to constrain the power-law exponent $n$ of the effective viscous flow law, we proceed by a forward operator that implements the simplest temperature-independent (isothermal) linear viscous (Newtonian) material ($n = 1$). The system of force-balance and constitutive equations are solved

195    numerically in two dimensions with the numerical FE code presented in Frehner et al. (2015).

Direct evidence from over-steepened rock glacier fronts, borehole deformation measurements (Arenson et al., 2002) and indirect geophysical investigations (Springman et al., 2012) suggest a pronounced thermo-mechanical layering of rock glaciers. A robust finding is that the deforming part can be divided into a sequence of three layers, surface boulder mantle, rock glacier core, and shear layer (Haeberli et al., 2006; Frehner et al, 2015; Cicoira et al., 2020). (1) The seasonally frozen

200    ice-free/poor surface layer consists of a matrix-poor, clast-supported framework of large, interlocked boulders (~active layer). Discrete movements of blocks in the boulder mantle are negligible compared to the total surface movement (but not with respect of inventories of cosmogenic nuclides, cf. Sect. 5.2). Deformation is accommodated by the ice-bearing interior that comprises the rock glacier core and the basal shear layer. (2) The ice-rich rock glacier core consists of a of a perennially frozen mixture of ice, debris, and fine material. (3) A fine-grained, few meters thick shear layer concentrates 60-90% of the

205    total displacement. Its higher deformation susceptibility, arising from the weakening effect of liquid water at grain boundaries, is in the model accounted by a lower viscosity. Boulder mantle, core and shear layer lie on an immobile

substratum of debris or bedrock. Over-steepened terrain steps, exposing the uppermost few meters of the stratigraphy, show the coarse boulder mantle over the finer-grained rock glacier core (cf. field observations in Sect. 4.1). Although no borehole deformation data is available for Bleis Marscha that could evidence the shear layer, we are confident that this typical rock

210 glacier feature does exist there. We approximate the deforming part of the rock glacier as a three-layer system consisting of a 5 m thick boulder mantle, 30–40 m thick core and a 3 m thick basal low-viscosity shear layer. The (variable) total thickness is estimated as follows: The model top boundary is the rock glacier surface given by the DEM, implemented as a free surface (Fig. 2b). The bottom boundary is defined by a fixed, no-slip boundary to the immobile substratum. Its elevation is projected from the adjacent terrain at the rock glacier front where the rock glacier rises from the Salteras trough shoulder (Fig. 2a; cf.

215 Kääb and Reichmuth, 2005; Scapozza et al., 2014) and parallel to the average rock glacier surface in the upper stretches. All layers including the ice-free boulder mantle effectively obey a viscous flow law and are separated by no-slip boundaries (dynamically coupled, "welded") (Arenson et al., 2002; Springman et al., 2012; Frehner et al., 2015).

We estimate the density of the rock glacier materials as the weighted average of the density of its constituents (Müller et al., 2016), namely debris (Err Granodiorite, $\rho_{debris}$ = 2700 kg m$^{-3}$), ice ($\rho_{ice}$ = 910 kg m$^{-3}$), and air ($\rho_{air}$ = 1 kg m$^{-3}$). For the

220 approximately void-free rock glacier core with 60 vol% ice, we obtain $\rho_c$ = 1626 kg m$^{-3}$, and for the boulder mantle with 30 vol% air $\rho_m$ = 1890 kg m$^{-3}$ (Barsch, 1996; Fig. 2b). The effect of water on density is insignificant. The prescribed viscosity ratios between the different layers are: rock glacier core to high-viscosity boulder mantle 1:20 (estimated from dominant wavelength of furrow-and-ridge microtopography, cf. back-of-the-envelope calculation below; Fig. 2b), and core to low-viscosity basal shear layer 10:1 (conservative assumption from the literature, cf. Cicoira et al. (2020) and references

225 therein). To estimate the effective viscosity ratio $R$ between the rock glacier mantle and core, we use an analytical formula based on buckle-folding theory that we apply to the furrow-and-ridge microtopography on units I–II (cf. Sec. 4.1; equation modified for one-sided support from Biot (1961); cf Frehner et al., (2015)):

$$R := \frac{\mu_m}{\mu_c} = \frac{3}{8}\left[\frac{\lambda_d}{\pi h_m}\right]^3. \tag{2}$$

The viscosity ratio $R$ can be calculated from the dominant wavelength $\lambda_d$ and rock glacier mantle thickness $h_m$. Inserting $\lambda_d$

230 = 50 m and $h_m$ = 4 m (estimates from field observations), we roughly estimate $R$ = 24.

The susceptibility for steady-state creep of debris-ice mixtures depends on debris-ice proportions (specifically the degree of ice supersaturation, i.e. the ice volume exceeding the pore volume), fabric, particle size, temperature and water content (Moore, 2014). Since the influence of each parameter is difficult to disentangle and the material properties and composition are not known at this level of detail, we absorb these contributions by the effective viscosity, $\mu$, and estimate it by solving the

235 inverse problem. We depart from an initial rock glacier model with a uniform viscosity of pure ice for the entire rock glacier core, $\mu_c^0 = 2 \times 10^{13}$ Pa s as an initial guess. Next, we compute synthetic surface velocity data by means of the discretized forward operator, carried out by the numerical FE code (Fig. 2c). The synthetic data predicted by the current model is

visually compared to the measured data, the orthophoto-derived surface creep rates. For rock glacier parts where the misfit between synthetic/predicted and measured data exceeds the data uncertainty, the viscosity is either increased if synthetic

240   velocities were too high compared to measured values ($d_{pred} > d_{meas}$) or decreased in the opposite case ($d_{pred} < d_{meas}$, estimation problem). The obtained plausible rock glacier viscosity distribution, $\tilde{m}$, that explains the measured surface velocities, $d_{meas}$, within their uncertainty, is one solution to the inverse problem.
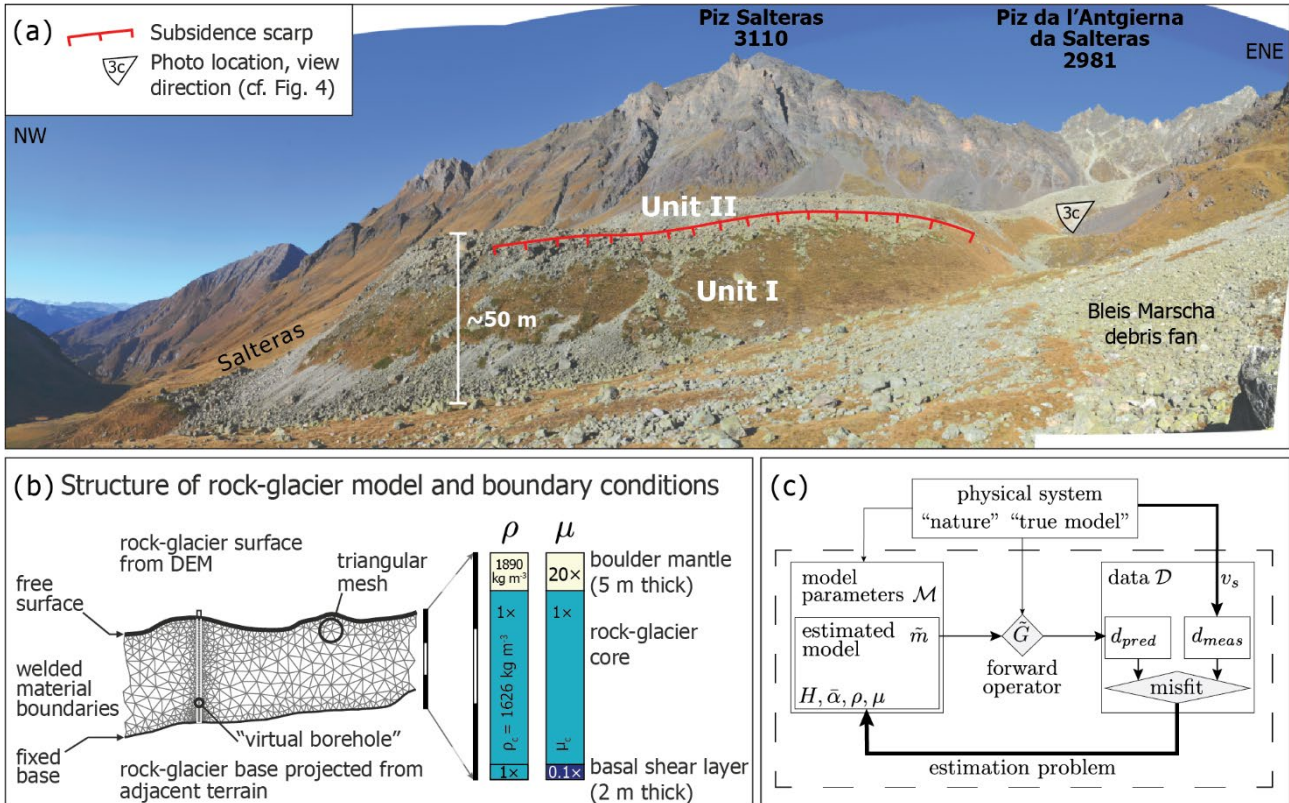
**Figure 2: (a)** Side view of the lowermost front, rising 30–50 m above the Salteras trough shoulder (cf. Fig. 4 for photo location and view direction). A stabilized, grassy sidewall extends upstream beneath younger lobes. The southernmost fringe is subsiding,
245   possibly due to ice loss. **(b)** Finite element (FE) model setup, triangular mesh (Shewchuk, 1996), boundary conditions, and prescribed ratios of density $\rho$ and dynamic viscosity $\mu$ (profiles). The surface boundary is the well-constrained elevation along a longitudinal profile, extracted from the DEM as a swath profile with TopoToolbox. The a-priori prescribed density and viscosity ratios create the characteristic mechanical layering of rock glaciers with a stiff, high-viscosity boulder mantle, deformable core, and basal weak, low-viscosity layer. **(c)** Inverse problem structure with the model parameters that are linked to the observable
250   data via the forward operator $\tilde{G}$, the FE model. The model predicts a synthetic surface velocity from the mechanical parameters that control the rock glacier creep: thickness H, average surface slope $\bar{\alpha}$, density $\rho$, and dynamic viscosity $\mu$.

## 4 Results and interpretation

### 4.1 Geomorphology of Bleis Marscha

255 The Bleis Marscha rock glacier is a tongue-shaped multi-unit or polymorphic (sensu Frauenfelder and Kääb, 2000) talus rock glacier at an elevation range of 2400–2700 m a.s.l. (Fig. 3). With a length of 1100 m, a width of 150–200 m, a surface area of ~$2.4 \times 10^5$ m$^2$, and a source area of ~$3.1 \times 10^5$ m$^2$, it ranks among the largest rock glaciers in the Err-Julier area. Based on an assumed mean thickness of 30-40 m, we estimate a total volume of ~$(7–10) \times 10^6$ m$^3$.
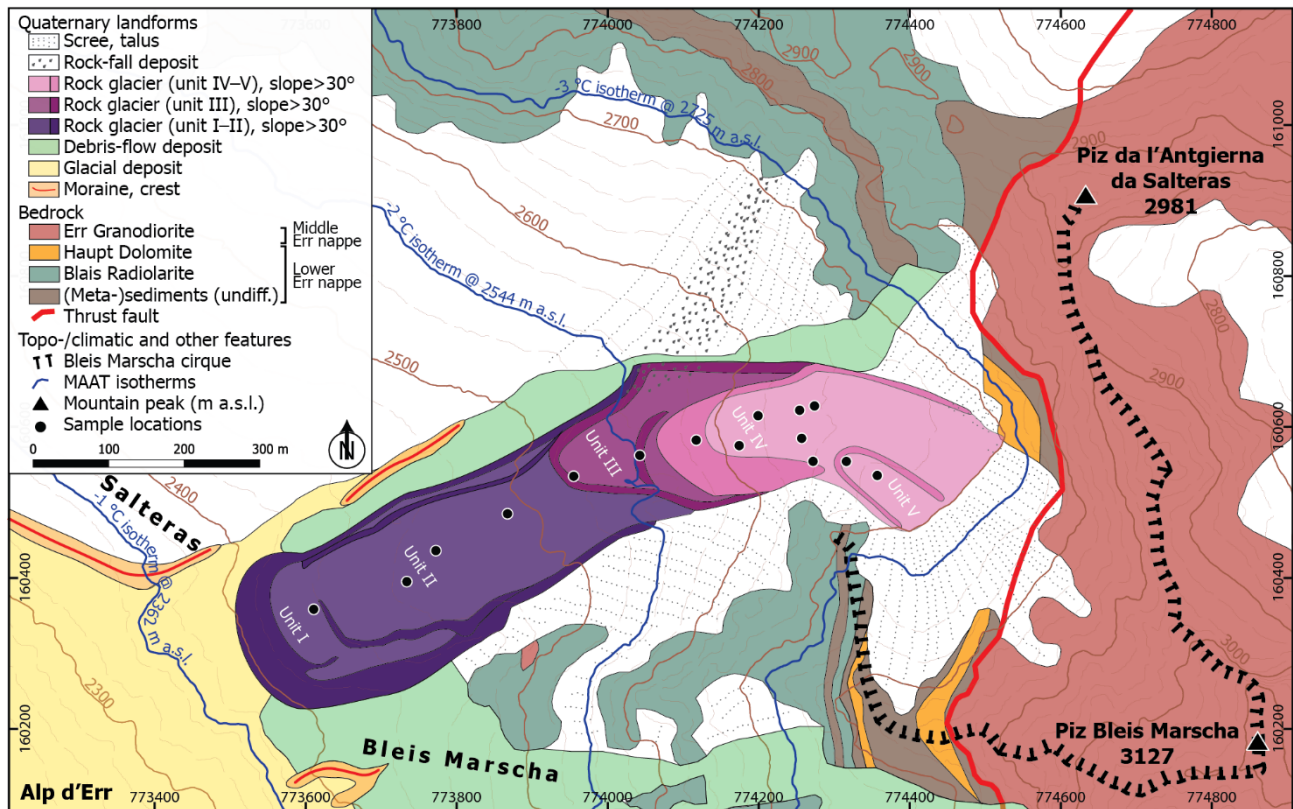
**Figure 3: Quaternary features and main lithologies in the Bleis Marscha cirque. Bedrock map modified from Cornelius (1932). A**
260 **subhorizontal thrust separates the crystalline Middle Err unit from the sedimentary Lower Err unit. Present-day MAAT isotherms are drawn according to Frauenfelder et al. (2001).**

The rock glacier boulder mantle consists of three main rock types, each with its source in different parts of the cirque headwall (Fig. 3, Cornelius (1932)): prevalently weathering-resistant Err Granodiorite, followed by Blais Radiolarite and tectonically fractured Haupt Dolomite. Weathering-prone lithologies such as rauhwacke (cellular dolomite), conglomerate,
265 limestone and shales occur only in lenses or thin seams in the headwall and are only rarely found on the rock glacier surface. Block volumes are typically between 0.5–50 m$^3$. Average block diameter is 1–2 m, exceptionally with >10 m edge length.

Size of the largest blocks increases in the direction of the rock glacier front. Downstream, the rock glacier rises over and is disconnected from the surrounding terrain.

Observations such as overall debris color reflecting differences in freshness of the sediment (weathering of the granite and lichen coverage), degree of soil development and internal steep frontal terrain steps (slope angle >30°) allowed us to subdivide the complex rock glacier into five different morphological units (Fig. 3) sensu Barsch (1996). These are labelled unit I (the lowest elevation, frontal part) to unit V (the highest elevation lobe). We interpret terrain steps as marking internal boundaries in the rock glacier related to overriding of lower lobes by higher lobes. The lower lobes must originally have been connected to the talus slopes in the Bleis Marscha cirque, the only source of Err Granodiorite, as testified by the dominance of Err Granodiorite (>80 vol%) increasing towards the lowermost rock glacier front. No large enough glacier existed throughout the Holocene to move debris out of the cirque. In theory, the lower lobes in part underlie the overriding higher lobes. Along its lower part (units I–II), the rock glacier lies on a till-mantled bedrock step (trough shoulder) known as Salteras. Schlosser (1990) mapped a right-lateral moraine near the trough shoulder break in slope (Fig. 3) and interpreted it as belonging to the Egesen stadial. The moraines and the rock glacier are nowhere in contact.

The lowermost front of the Bleis Marscha rock glacier rises roughly 30–50 m from edge of the Err valley trough shoulder at an elevation of 2380 m a.s.l. (Fig. 2a). The frontal part, denoted as unit I (Figs. 3, 4), exhibits several features suggesting that it is apparently inactive (cf. Sect. 4.3). This includes signs of settling thus incipient degradation of the rock glacier body, patches of vegetation and marked soil development, as well as extensive lichen cover, iron staining and weathering rinds. Yet, a frontal boulder apron indicates that the movement of this apparently old body has not ceased completely. The boundary between unit I and II is a steep, ca. 2–3 m high terrain step, that extends upstream as a stable, grassy sidewall along the two lobes (margin of unit I, Fig. 2a). Where unit II rests on unit I, it is recessed by ~5 m forming a ledge along the sides (Fig. 5c). The boulder weathering and abundance of black and green lichen give the lower lobes (units I–II) a much darker brownish grey appearance in comparison to the higher elevation lobes. Blocks in units I–II are subangular to subrounded; weathering of the Err Granodiorite blocks plays an important role. The surface of unit II is gently inclined (~10°), with a well-developed furrow-and-ridge microtopography of down-stream crescent-shaped transverse ridges that are regularly spaced about 50 m apart and separated by <5 m deep furrows (Fig. 5b). The mean rock glacier surface slope and presumably also the basal slope steepens from ~10° to 20° at an elevation of 2500 m a.s.l., causing units I–II to decelerate. The break in slope induced along-flow compressive stresses (Fig. 5b). Buckle folding of the layered rock glacier (stiff boulder mantle, deformable ice-rich core) in response to compressive flow likely was the dominant formation mechanism of the transverse furrow-and-ridge microtopography of unit II (cf. Frehner et al., 2015; Sect. 3.4).

Along the left-lateral side of units I–II, a WSW-ENE running scarp indicated by exposed fresh material dissects both units and is therefore a younger feature. The southernmost fringe of the rock glacier is slowly subsiding. Debris slides or aprons do not follow along the entire scarp. The slow, interior deformation must originate at depth rather than at shallow levels,

what would push loose surface debris over the edge. The body is sagging instead of laterally advancing, for which ice loss is a possible explanation.

Unit III is clearly differentiated from units I–II by the slightly paler color of the debris (less brown) and by a steep, 5 m high, frontal terrain step (Fig. 5b). This terrain step is quite marked; the grass cover and soil development suggest long-term stability. The incipient soil development and vegetation patches, clearly differentiate unit III from the upper units IV and V. The right-lateral boulder apron along unit III between the rock-fall deposits and its front formed by debris slides pours fresh material over a stabilized, grassy sidewall, which suggests recent activity of unit III (Fig. 5c). Units I–III are bordered by a stable lateral ridge which is densely vegetated and has a thick soil cover (Figs. 5b, c). It extends upslope until the body disappears beneath the younger unit IV (Fig. 2a). We interpret this grassy ridge as the margin of the oldest, possibly relict body (unit I) that underlies the younger lobes (units II and III), and not as lateral moraines (Frauenfelder et al., 2001; cf. Barsch 1996).

The boundary between unit III and IV is another steep 5 m step in the terrain. The steep (>20°) terrain here is cut by three major scarps where the two-layered stratigraphy of a coarse, clast-supported blocky mantle (thickness of ~3 m) over a finer, matrix-supported core is exposed. These inner terrain steps are expressions of discontinuities and form the frontal boundary of units III and IV (Fig. 5b). Units IV–V are starkly different in appearance from units I–III. Again, the hue of the debris lightens (more grey than brown), the debris is much less weathered, boulders are more angular. The maximum block size decreases from 5–6 m in diameter to 2–3 m. Vegetation and soil patches are lacking. Unit IV exhibits several longitudinal ridges along the right-hand side (Fig. 4). In the bend at the lip of the cirque, the microtopography becomes more accentuated with a set of parallel longitudinal, asymmetric ridges (steep side facing outwards), whose amplitude however rarely exceeds 2 m. These are flow features that likely relate to the left turn that the rock glacier makes here. Unit V, a small rock glacier lobe (width 80 m), is well visible in the root zone emanating from the talus slope (Figs. 4, 5a).

We observed neither signs of glacier activity nor any surface ice remaining from the recent glaciation of the cirque (Dufour, 1853; Siegfried, 1887). The "small ice patch" mentioned by Frauenfelder et al. (2005) was no longer visible in 2017. The smooth, unstructured talus passes directly into the broad (180 m) rock glacier root zone (unit IV) at an elevation of 2700 m a.s.l. (Fig. 5a). No morphological evidence of the recent LIA glacier remains.
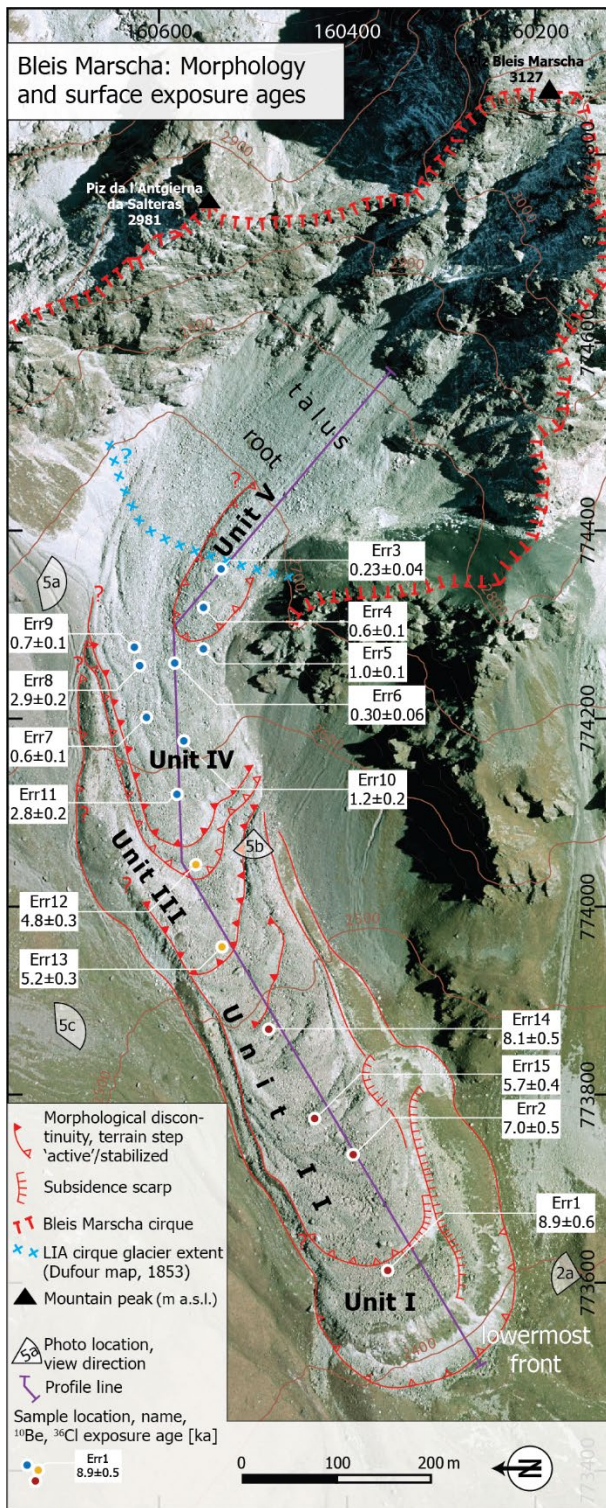
**Figure 4: Plan view of morphological domains on 2003 orthophoto showing the morphological discontinuities (inner fronts/terrain steps, slope breaks), sampling locations and exposure ages (cf. Fig. 8 for surface creep rates). Bleis Marscha is a stack of three overriding lobes composed of units I–II, unit III, and units IV–V, separated by terrain steps. Historical maps suggest that the Holocene maximum extent of the cirque glacier, reached during the Little Ice Age (LIA) around CE 1850, remained within the Bleis Marscha cirque. (Orthophoto reproduced with the authorization of the Swiss Federal Office of Topography swisstopo).**

335
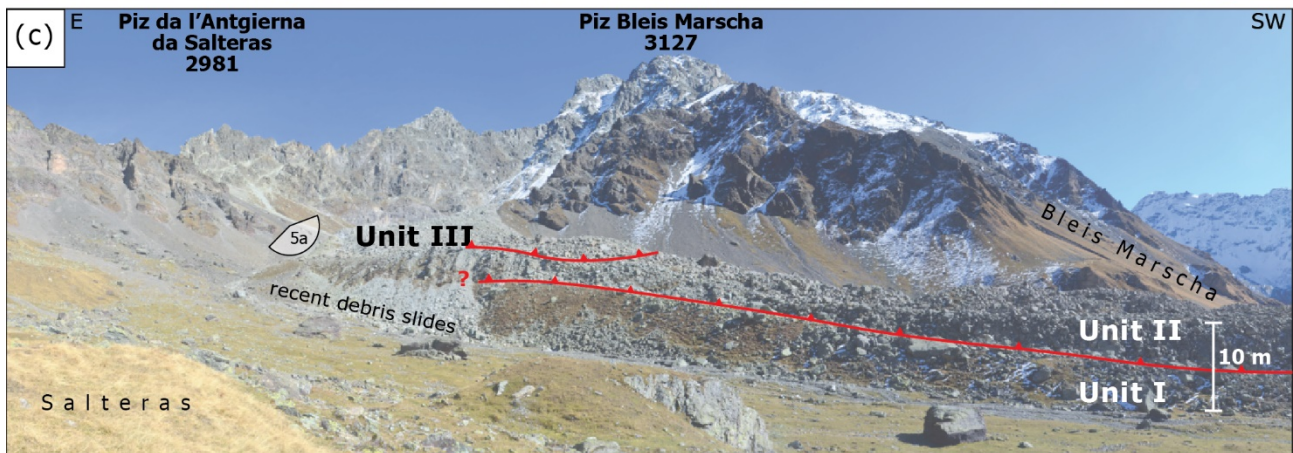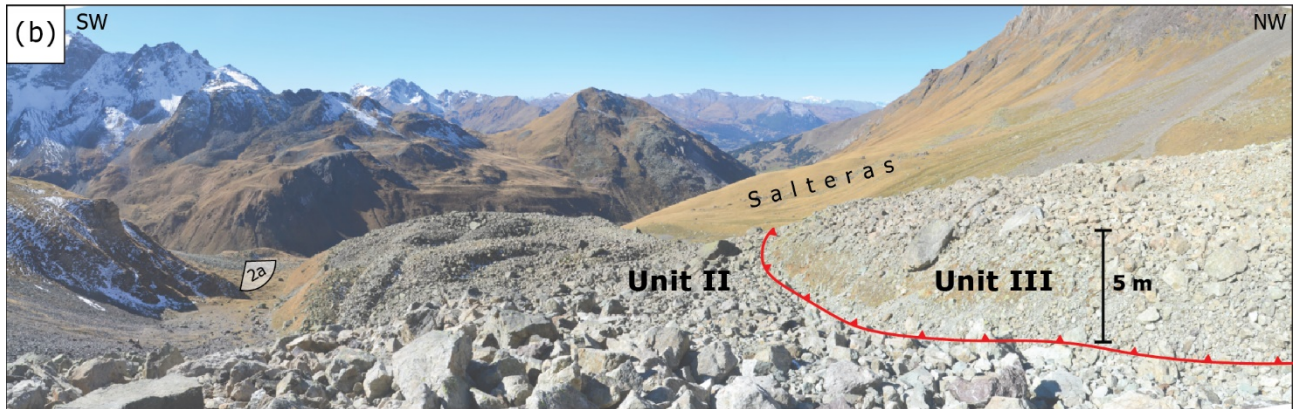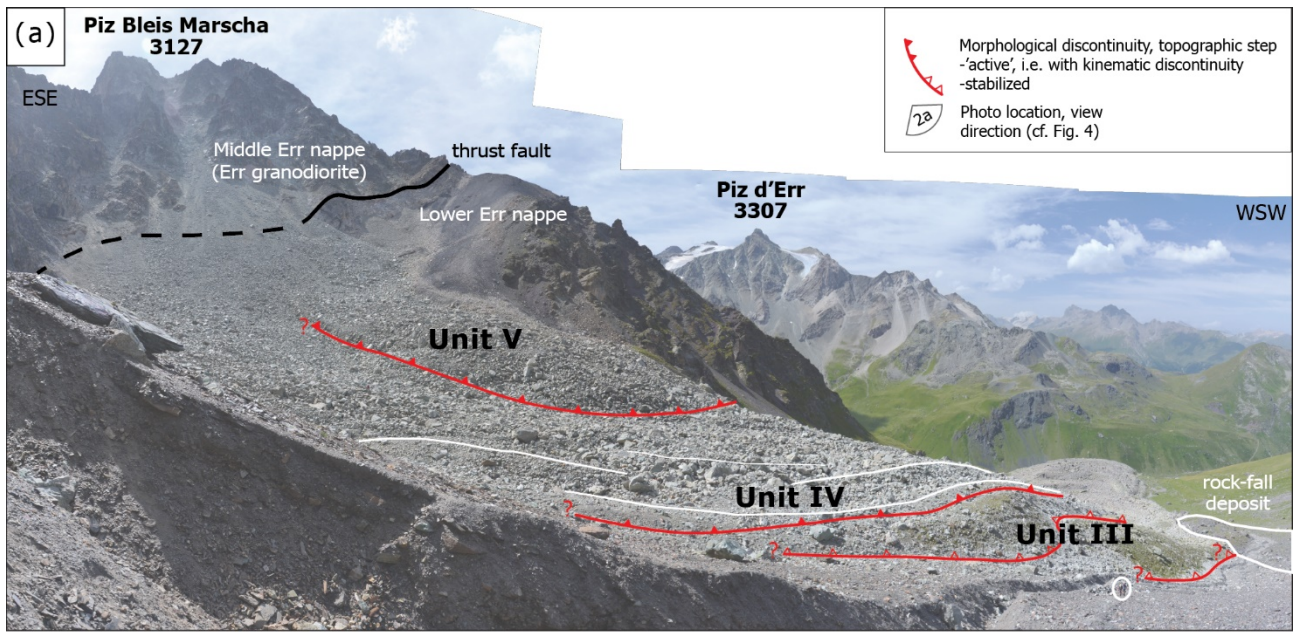
**Figure 5: Panorama images of the Bleis Marscha rock glacier (cf. Fig. 4 for photo locations). (a) View to SE into the root zone in Piz Bleis Marscha cirque. The dominant lithology of the boulder mantle, Err Granodiorite, is sourced above the thrust fault in the back of the cirque. Photo taken in August 2018. (b) View to W onto lower rock glacier part with furrow-and-ridge microtopography (unit II). The currently advancing unit III is outlined by the prominent terrain step. Photo taken in October 2018. (c) Side view to SE of the middle rock glacier part, evidencing the Bleis Marscha rock glacier as a multi-unit debris stream composed of multiple stacked lobes. The fresh lateral debris apron along unit III hints at ongoing activity. Unit I at the base of the stack is discernible by the stable, grassy sidewall and the ledge beneath unit II. Photo taken in October 2018 .**

## 4.2 Boulder exposure ages

Measured $^{10}$Be concentrations are in the range of $(0.7 \pm 0.1$ to $23.6 \pm 1.2) \times 10^4$ at g$^{-1}$. The measured $^{36}$Cl concentration is $(3.1 \pm 0.1) \times 10^5$ at g$^{-1}$ (Tables 1, 2). Cosmogenic nuclide exposure ages ($^{10}$Be and $^{36}$Cl) range from $0.23 \pm 0.04$ to $8.95 \pm 0.64$ ka (Figs. 4, 7; Tables 1, 2).

For the lowermost, oldest part of the rock glacier (unit I), we obtained one $^{10}$Be exposure age: Err1 at $8.95 \pm 0.64$ ka (Figs. 4, 6a, 7). The three ages for unit II are, from lowest elevation to highest, $7.03 \pm 0.51$ ka (Err2, Fig. 6b), $5.70 \pm 0.40$ ka (Err15, Fig. 6c) and $8.08 \pm 0.46$ ka (Err14, Fig. 6d). From the next higher unit III, we obtained two $^{10}$Be ages: $5.17 \pm 0.35$ ka (Err13, Fig. 6d) and $4.80 \pm 0.33$ ka (Err12, Fig. 6e). In the higher elevation, more active parts of the Bleis Marscha rock glacier, nine ages were determined, seven from unit IV and two from unit V. The $^{10}$Be ages for unit IV are from lower to higher elevation, Err11 at $2.77 \pm 0.17$ ka (Fig. 6f), Err10 at $1.18 \pm 0.16$ ka, Err7 at $0.65 \pm 0.06$ ka, Err6 at $0.30 \pm 0.06$ ka, Err9 at $0.73 \pm 0.08$ ka and Err5 at $1.00 \pm 0.08$ ka. The $^{36}$Cl age for a dolomite boulder in unit IV is $2.89 \pm 0.18$ ka (Err8, Fig. 6g). The ages from the highest youngest lobe, unit V, are $0.56 \pm 0.06$ ka for Err4 and $0.23 \pm 0.04$ ka for Err3 (Fig. 6h).

Ages generally decrease from the lowermost toe of the rock glacier (unit I) to the uppermost lobe (unit V). Nevertheless, ages on different morphological units show a degree of 'geologic scatter'. In stark contrast to nearly all exposure dating projects whereby the cosmogenic nuclide concentration records the time elapsed since the boulder has reached its final position (e.g. on a moraine or a landslide deposit), we have dated an active, moving landform. This requires a different way of looking at the exposure dates. The cosmogenic nuclide concentrations comprise all the nuclides acquired during exposure of the sampled surfaces. This includes in the bedrock (inheritance), at the talus foot, on the rock glacier surface including while it is moving and at the final boulder position. Effects already discussed in other studies (Heyman, 2011) such as boulder rolling, toppling or spalling can also affect the nuclide concentration. This is discussed in detail in Sect. 5.2.
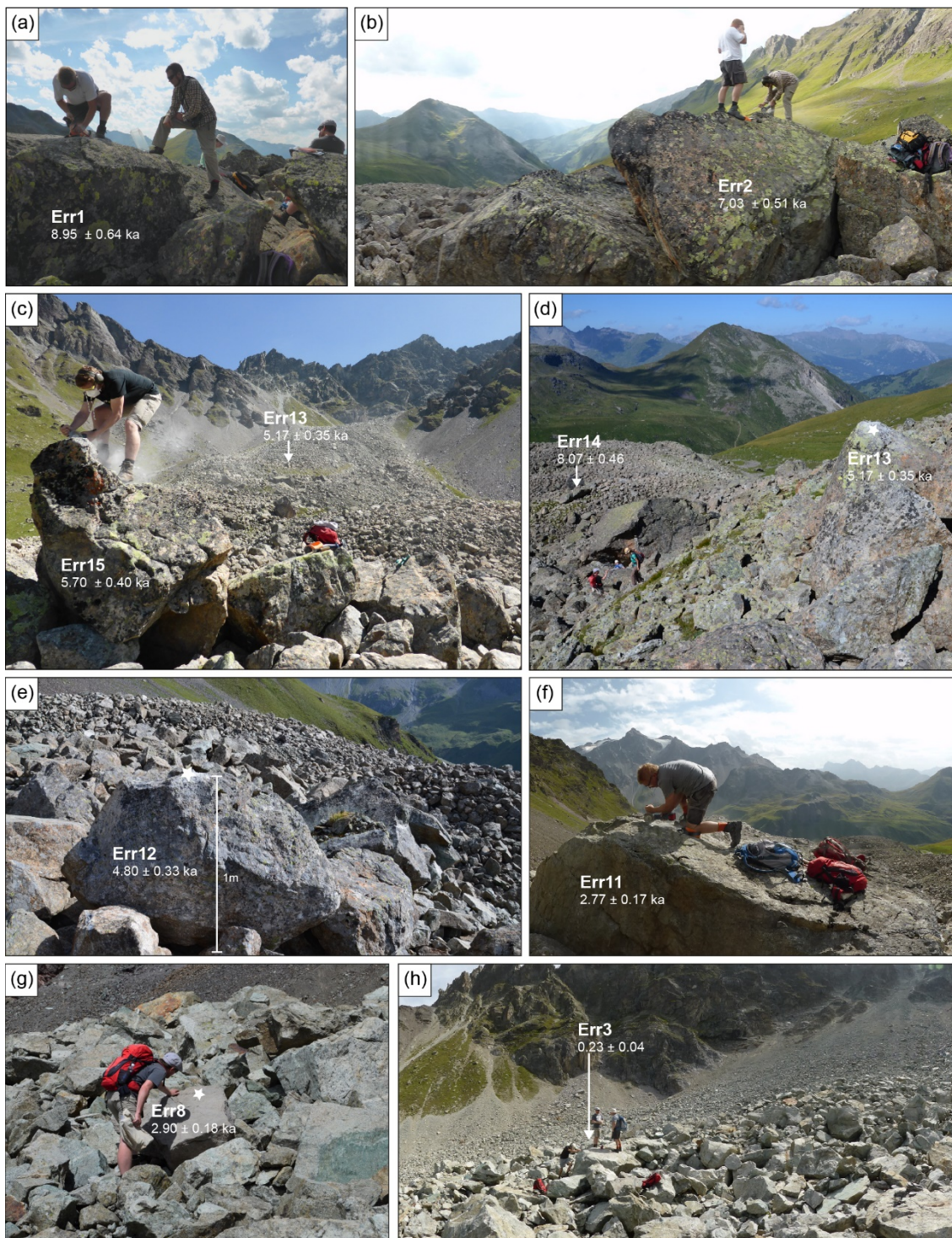
**Figure 6: Field photographs of selected sampled boulders that are discussed in the text. In panels (d, e, g), the star marks the sampled surface.**

**Table 1:** [10]Be sample information of the Bleis Marscha rock glacier boulders (Err Granodiorite) with location, sample information, blank corrected AMS [10]Be concentration and calculated exposure age.

| Sample name | Latitude | Longitude | Elevation | Sample thickness | Shielding factor[a] | [10]Be concentration[b] | Exposure age[c], erosion corrected |
|---|---|---|---|---|---|---|---|
| | °N | °E | m a.s.l. | cm | - | $10^4$ at g$^{-1}$ | a |
| Err1 | 46.5719 | 9.7036 | 2448 | 1.5 | 0.9739 | 23.584 ± 1.216 | 8948 ± 466 (636) |
| Err2 | 46.5723 | 9.7053 | 2482 | 1.5 | 0.9751 | 18.992 ± 1.004 | 7027 ± 374 (505) |
| Err15 | 46.5727 | 9.7057 | 2483 | 1.0 | 0.9582 | 15.257 ± 0.771 | 5697 ± 290 (399) |
| Err14 | 46.5730 | 9.7070 | 2498 | 2.0 | 0.9484 | 21.366 ± 0.638 | 8076 ± 243 (460) |
| Err13 | 46.5734 | 9.7081 | 2529 | 2.0 | 0.9502 | 14.027 ± 0.659 | 5169 ± 244 (349) |
| Err12 | 46.5737 | 9.7093 | 2552 | 1.5 | 0.9476 | 13.234 ± 0.654 | 4796 ± 238 (332) |
| Err11 | 46.5738 | 9.7102 | 2583 | 1.5 | 0.9450 | 7.819 ± 0.277 | 2774 ± 99 (166) |
| Err10 | 46.5737 | 9.7110 | 2612 | 1.5 | 0.9211 | 3.308 ± 0.425 | 1181 ± 152 (162) |
| Err7 | 46.5740 | 9.7113 | 2623 | 1.5 | 0.9365 | 1.854 ± 0.161 | 646 ± 56 (64) |
| Err6 | 46.5738 | 9.7120 | 2643 | 2.0 | 0.9406 | 0.860 ± 0.183 | 295 ± 63 (64) |
| Err9 | 46.5742 | 9.7124 | 2650 | 1.5 | 0.9204 | 2.083 ± 0.213 | 727 ± 74 (82) |
| Err5 | 46.5735 | 9.7122 | 2647 | 1.5 | 0.9428 | 2.940 ± 0.202 | 1001 ± 69 (84) |
| Err4 | 46.5735 | 9.7127 | 2665 | 2.0 | 0.9392 | 1.642 ± 0.154 | 556 ± 52 (59) |
| Err3 | 46.5733 | 9.7133 | 2680 | 1.8 | 0.9259 | 0.673 ± 0.115 | 229 ± 39 (41) |

a Shielding correction includes the topographic shielding due to surrounding landscape and the dip of the sampled surface.

b AMS measurement errors are at 1σ level and include the AMS analytical uncertainties and the error of the subtracted blank. Measured ratios were measured against the in-house standard S2007N which is calibrated to 07KNSTD.

c Exposure age errors are internal errors (uncertainties represent 1σ confidence range comprising AMS counting errors and errors based on the normalization to blanks and standards). External errors are given in parentheses. Erosion correction for a surface erosion rate of 1 mm kyr$^{-1}$.

**Table 2:** [36]Cl sample information of the Bleis Marscha rock glacier boulder (Haupt Dolomite) with location, sample information, blank corrected AMS [36]Cl concentration and calculated exposure age.

| Sample name | Latitude | Longitude | Elevation | Sample thickness | Shielding factor[a] | Cl in rock | [36]Cl concentration[a,b] | Exposure age[c], erosion corrected |
|---|---|---|---|---|---|---|---|---|
| | °N | °E | m a.s.l. | cm | - | ppm | $10^6$ at g$^{-1}$ | a |
| Err8 | 46.5741 | 9.7120 | 2643 | 1.5 | 0.937 | 49.63 ± 0.09 | 0.313 ± 0.014 | 2890 ± 130 (181) |

a Concentration measured against [36]Cl/Cl standard K382/4N (Christl et al., 2013; Vockenhuber et al., 2019).

b Sample ratio corrected for laboratory blank of (2.5 ± 0.4) × 10$^{-15}$ [36]Cl/[35]Cl.

c Production rates as in Alfimov and Ivy-Ochs (2009) and references therein. Erosion correction for a surface erosion rate of 5 mm kyr$^{-1}$ (karst weathering/corrosion).

**Table 3:** Elemental composition of the dolomite sample Err8.

| SiO2 | Al2O3 | Fe2O3 | MnO | MgO | CaO | Na2O | K2O | TiO2 | P2O5 | LoI | Sm | Gd | Th | U |
|------|-------|-------|-----|-----|-----|------|-----|------|------|-----|-----|-----|-----|-----|
| % | % | % | % | % | % | % | % | % | % | % | ppm | ppm | ppm | ppm |
| 0.45 | 0.35 | 0.26 | 0.06 | 20.39 | 31.88 | 0.06 | 0.10 | 0.01 | 0.01 | 46.12 | 0.20 | 0.10 | 0.20 | 6.70 |
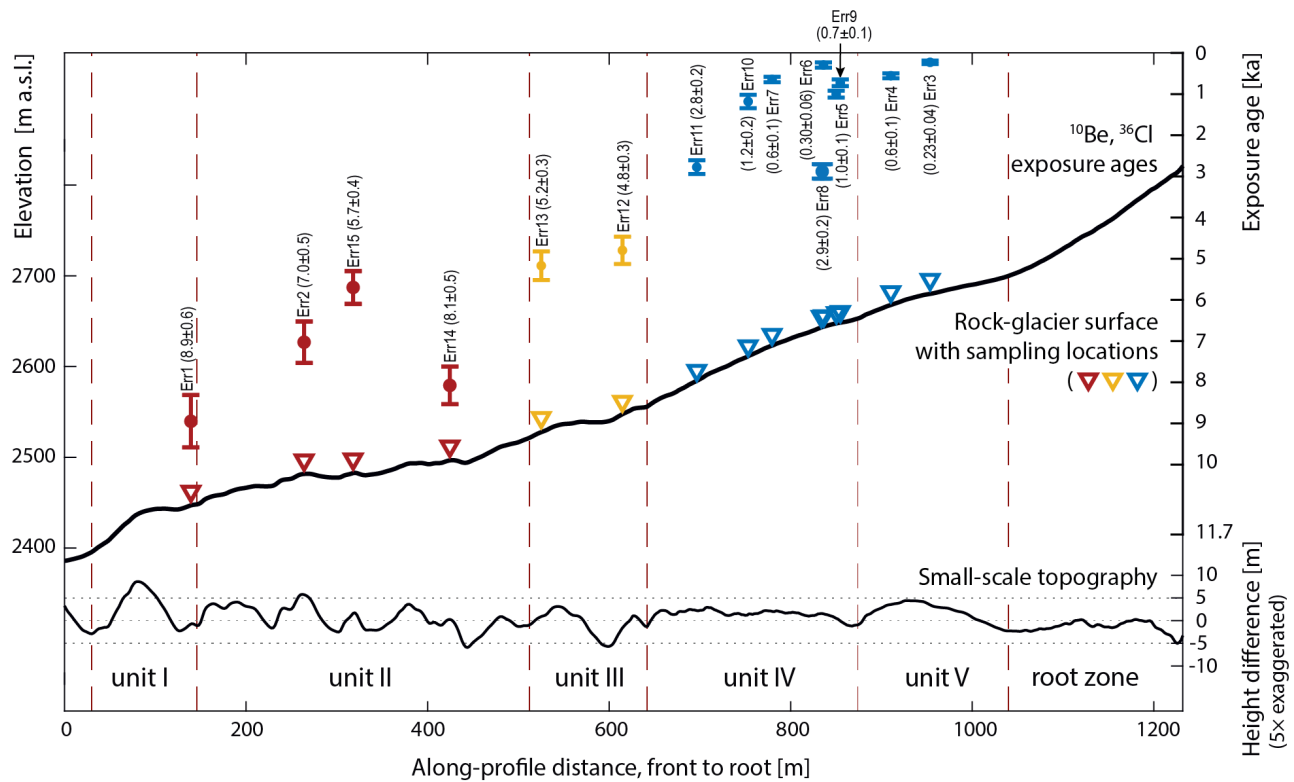
**Figure 7: Longitudinal section of rock glacier surface along the profile line shown in Fig. 4 showing exposure ages, sample location**
**(triangles), surface elevation, small-scale topography, and morphological units (red dashed lines). Note the "stratigraphically"**
**directed time axis to emphasize the general anti-correlation of the exposure ages with altitude. Exposure ages and sampling**
**location are projected perpendicular onto the longitudinal profile, not along (unknown) surface isochrons. The small-scale**
**topography is a high-pass filtered topography computed by subtracting a 100 m running mean from the altitude at each point.**

## 4.3 Modern surface creep rates

Two orthophotos from late summer 2003 and 2012 are matched. The result is a noise-filtered horizontal surface creep-rate field for the Bleis Marscha rock glacier and its immediate surroundings (Fig. 8). Surface creep rates are in the range $v_s \approx 25$–$60$ cm a$^{-1}$. There are data gaps where the image correlation failed due to decorrelation (non-translational movement, toppling, or vegetation), or inadequate input images (textureless snow fields). Since considerable presumably stable adjacent off-rock

glacier areas show apparent surface movements of up to 15 cm a$^{-1}$, we adopt this conservative value as the significance level.

395    Areas with speeds lower than this level of detection are classified as non-moving (dark grey areas in Fig. 8).

The lowermost unit I is mostly below the level of detection and considered close to immobile. Surface creep rates increase gradually upslope to 25 cm a$^{-1}$ on unit II, while the creep pattern changes: From slow deformation of a central, narrow stripe with outwards gradually decreasing creep rates to a laterally sharply confined, lobe-wide en bloc movement. On units II–IV, surface creep rates increase more stepwise up to 60 cm a$^{-1}$ until the mid-section of unit IV, along with the average surface

400    slope (Fig. 10b). The 'steps' or decorrelation gaps in surface speed coincide with terrain steps that delimit the lobes laterally and frontally. This suggests differential movement of the lobes that override each other, agreeing with field observations of boulder toppling at the over-steepened, 'active' terrain steps (Fig. 4). Important discontinuities are in front of unit III (Fig. 5b) and unit IV (cf. Figs. 7, 10b). Towards the talus, surface creep rates decrease. The orographic left side of the root zone, where unit V is, is more active.

405    Data points from the entire rock glacier surface drawn in a slope–surface creep rate scatter plot (average slope within 100 m radius, Fig. 9, grey dots) are clustered in a wedge-shaped domain; the few outliers are due to non-translational movement (e.g. sliding, tumbling) and not due to large-area cohesive creep. Higher creep rates are reached at higher surface slope angles, in accordance with the concept of shear-stress driven creep. A clearer slope-velocity relation emerges when data from a 20 m wide stripe along the central profile are highlighted (Fig. 8), because they are unaffected by boundary effects such as

410    lateral drag and non-translational movements. The clear correlation between creep rate and average surface slope suggests that surface creep rates on units II–IV (altitude bands 2475-2653 m asl.) are controlled by topography (via average surface slope) rather than by material property (e.g. effective viscosity). The correlation is lost on the lowermost frontal area (lowermost ~100 m, unit I), where incipient stabilization and possibly loss of ice hampers viscous creep, and on the uppermost unit V, possibly because slope-independent deformation processes other than creep are dominant (cf. Fig. 10b).

415    We explore the relation between surface creep rate, topography and material properties numerically in the next chapter.
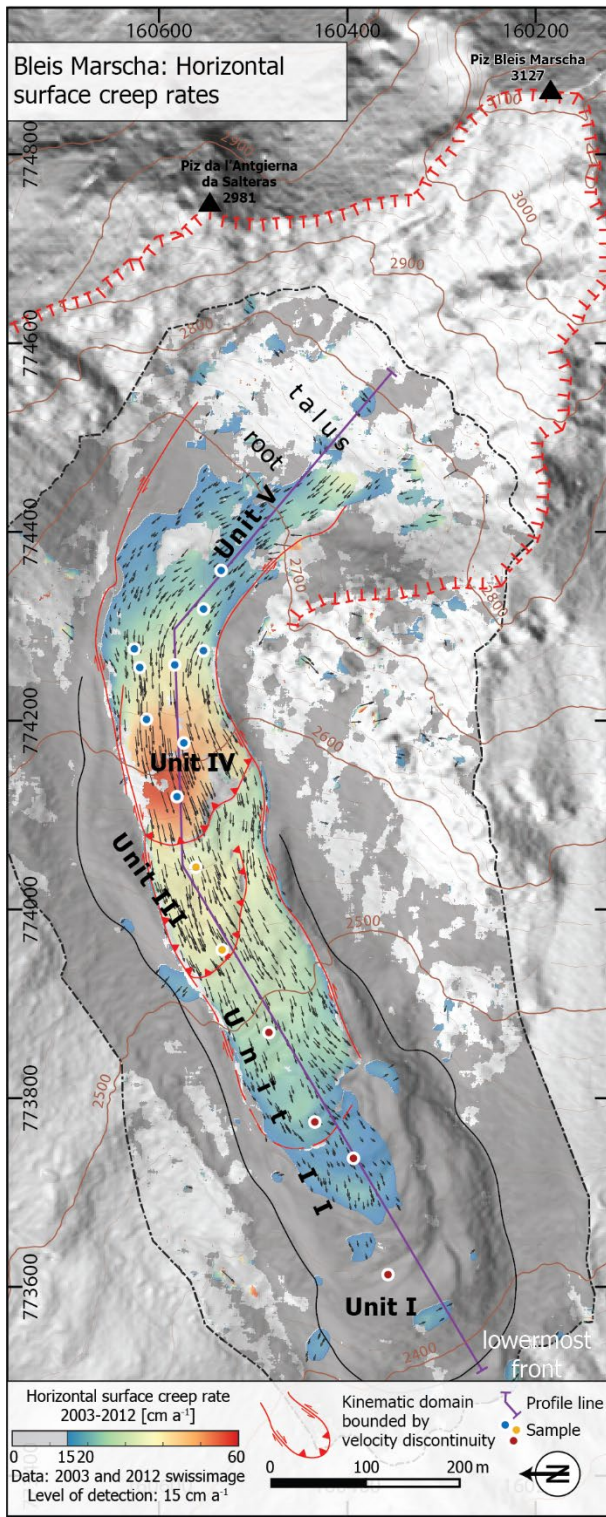
**Figure 8: Modern horizontal surface creep rates, derived from two orthophotos from 2003 and 2012. Level of detection is 15 cm a⁻¹. The long temporal baseline of nine years averages inter-annual variabilities in rock glacier creep rates, and is a robust estimate of modern, short-term surface kinematics. Morphological (cf. Fig. 4) and kinematic discontinuities (decorrelation gaps and "jumps" in creep rates) largely coincide. Areas below the level of detection are considered immobile except for the lowermost front (unit I), where a fresh frontal boulder apron and comparison with the 1988 orthophoto indicates slow surface movement (5–10 cm a⁻¹). (Hillshade background map reproduced with the authorization of the Swiss Federal Office of Topography swisstopo).**
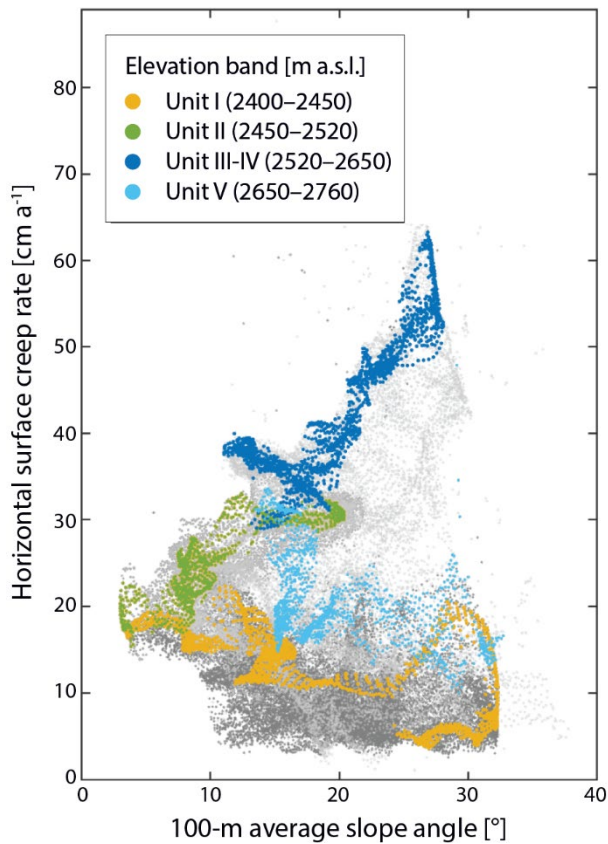
**Figure 9: Slope–creep rate relation:** Scatter plot showing the correlation between the 100 m averaged slope (from smoothed DEM) and the horizontal surface creep rate for different elevation bands of the Bleis Marscha rock glacier. The grey dots are data points from the entire rock glacier (lowermost part <2450 m asl. in dark grey, lobes >2450 m asl. in light grey). Data points restricted to a 20 m stripe along the central profile, where the effect of lateral drag is minimal, are colored. The good correlation between surface slope and surface creep rates suggests that on units II–IV, topographically controlled creep is the dominant deformation mechanism.

## 4.4 Controls on modern surface creep rates

For a given rock glacier thickness, layering, and density, the effective viscosity distribution is fitted to the 2003/2012 surface creep rates. We obtain a simplified, but plausible rock glacier structure (Fig. 10a) that reproduces the image-correlation data within their uncertainty (Fig. 10b). The result suggests that the viscosity in the more slowly moving, apparently inactive low-elevation lobes are only slightly higher than in the active, more rapidly moving high-elevation lobes (Fig. 10a), i.e. that surface creep rates on units II–IV can be explained by topographical parameters (thickness, surface slope) alone. In contrast, the external parts of unit I move more slowly than potentially possible given the comparable surface slope and thickness as unit II. This modelling result corroborates our hypothesis of topographically-controlled creep on units II–IV and incipient degradation of unit I.

We used the FE code presented in Frehner et al. (2015). The aspects discussed therein (incompressibility, boundary effects) apply analogously in this study. Our synthetic vertical deformation profiles ("virtual boreholes", Fig. 10a, insets) resemble measured borehole deformation profiles from other rock glaciers (Arenson et al., 2002). No boreholes have been drilled on Bleis Marscha rock glacier. Although the simple Newtonian continuum model with vertical viscosity layering does not accurately reproduce deformation mechanisms at the micro scale, it does capture the essential deformation effects that lead to the observed surface creep rates.

The solution to Eq. (1) is non-unique, inasmuch as higher surface speed can be achieved with any combination of greater thickness, steeper surface slope, or lower viscosity. Large errors in the topographical parameters would undermine the goal of separating topographical from material controls. However, the driving stress and ultimately the deformation is largely governed by the well-constrained average surface slope (not by the basal slope (Nye, 1952)) and the reasonably assessable rock glacier thickness and density. The remaining unknown viscosity can be estimated with sufficient accuracy.
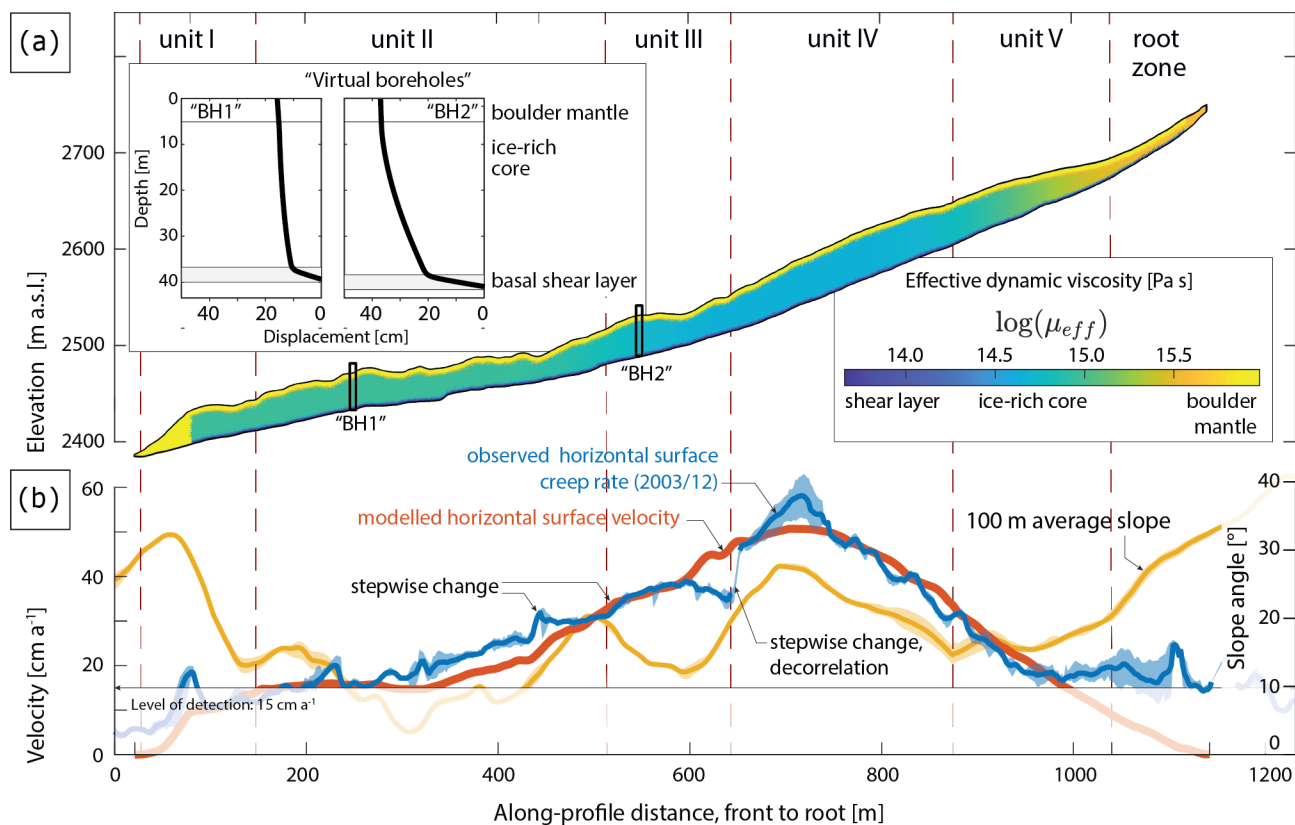
Figure 10: (a) Inferred effective viscosity distribution on the longitudinal transect (profile line shown in Figs. 4, 8). The inferred effective dynamic viscosity does not vary significantly over units II–IV. Along-profile variations in surface creep rates are primarily controlled by the surface slope. Insets: Modelled yearly horizontal displacements in "virtual boreholes". The strain localization near the base despite the linear stress–strain rate relationship arises from the rock glacier parameterization with the three-part mechanical layering (boulder mantle, core, basal shear layer). The simple Newtonian model with depth-varying viscosity generates synthetic velocity profiles that resemble borehole deformations measured on other rock glaciers.

**(b) Longitudinal section of observed surface creep rate (blue line), modelled/synthetic (orange) horizontal surface velocity and the 100 m filtered slope (yellow). Horizontal surface creep rate of sections dominated by viscous creep roughly follow the average surface slope (units II–IV). Correlation is lost on the lowermost front and talus. The morphologically-defined units I–II, unit III, and units IV–V are separated by sharp speed gradients ('kinematic discontinuities', dark red triangles, cf. Fig. 10).**

## 5 Discussion

By examining the exposure ages and considering the image correlation results we decipher the history of the Bleis Marscha rock glacier over the past 9 ka and put in into the framework of the known regional climate history (Ivy-Ochs et al., 2009; Böhlert et al., 2011a).

### 5.1 Exposure dating an active rock glacier

Cosmogenic nuclide ages include all of the time that a rock surface is exposed to cosmic rays. However, in nearly all previous studies, the age sought encompasses only the nuclides produced since the boulder has reached its final position (e.g. in a moraine or landslide deposit). Unlike single-age landforms that for the most part formed in short-lived events, active rock glaciers are continually moving and grow over centuries–millennia. Rock surfaces are exposed to cosmic rays in various stages of the landform evolution.

Rock glaciers form on an inclined slope (e.g. talus) when an accumulation with favourable debris-ice proportions reach a critical thickness (cf. Kirkbride and Brazier, 1995; Haeberli et al., 2003, 2006). Viscous creep emerges as the dominant deformation mechanism and the mobilized material begins to creep down-slope under its own weight. Coarse blocks on the rock glacier surface, that form the boulder mantle, are sourced in the rock glacier root and carried towards the front. Conceptually, boulder residence time on the rock glacier surface is the time since initial deposition in the rock glacier root and comprises the travel time (creep-induced, passive transportation during active periods) and, for an inactive–relict landform, time since stabilization of the landform (relict period) (Haeberli et al., 1998, 2003). This model predicts a spatially correlated age signal with downstream systematically increasing surface ages. The 'conveyor belt'-like advance mechanism affects the rock glacier age structure and the relations between surface velocity, length, and age (Kääb et al., 1997; Kääb and Reichmuth, 2005). Due to the decrease of horizontal speeds with depth and the frontal volume loss mainly from excess ice meltout, the rock glacier surface moves faster than the advancing landform itself (Haeberli et al., 1998; Frauenfelder et al., 2005; Kääb and Reichmuth, 2005). Surface exposure ages atop the front of rock glaciers give the lower bound of the landform age (cf. Scapozza et al., 2014; Winkler and Lambiel, 2018).

On an active rock glacier, the cosmogenic nuclide concentration adds up all of the following periods of exposure (Table 4):

1.  Pre-exposure in the headwall (bedrock inheritance),
2.  Transit time in the talus or during intermediate storage upstream in the talus,
3.  Transport on the moving (active) rock glacier (travel time),
4.  Sitting at the (quasi-)stabilized position (inactive rock glacier or relict rock glacier deposit).

As in other cosmogenic nuclide studies, post-depositional surface processes like boulder surface weathering, spalling, unaccounted for shielding, rotation and toppling lead to a lower total boulder nuclide inventory (Ivy-Ochs et al., 2007; Heyman, 2011).

**Table 4:** Processes that affect measured cosmogenic nuclide concentration in a boulder on an active rock glacier (see text for discussion). Surface processes like exposure in the bedrock (inheritance), post-depositional weathering, spalling, unaccounted for cover or shielding, rotation and toppling affects single boulders to variable degrees and largely independently from their neighbors.

| Process | Effect on nuclide inventory and exposure age |
|---|---|
| **Ideal nuclide buildup**<br>'$^{10}$Be, $^{36}$Cl clock' dates the onset of boulder travel in the rock glacier root | Ideal nuclide inventory: travel time and time elapsed since rock glacier stabilization |
| No inheritance, immediate deposition on rock glacier root with rapid (or buried) transfer in talus, exposure during transport embedded in boulder mantle, fixed boulder orientation, continued exposure after rock glacier advance stops | Complete record of (1) transport on advancing rock glacier, and (2) sitting at (quasi-) stabilized position on inactive rock glacier or relict rock glacier deposit |
| **Pre-depositional effects**<br>'$^{10}$Be, $^{36}$Cl clock starts too early' | Inherited nuclides or excess nuclides from previous exposure, 'too old' exposure ages |
| Exposure in rock wall (bedrock inheritance) | Higher nuclide concentration |
| Exposure during upstream storage prior to deposition on rock glacier, e.g. in talus or moraine | Higher nuclide concentration |
| **Post-depositional effects**<br>'slowing or resetting the $^{10}$Be, $^{36}$Cl clock' | Nuclide concentrations lower compared to 'true' exposure time, 'too young' exposure ages |
| Boulder instability: rotation, toppling or overturning, relocation | Lower nuclide concentration from changing dip and orientation of surface, incomplete exposure (self-shielding) to variable degree |
| Spalling | Lower nuclide concentration |
| Surface weathering (erosion) | Lower nuclide concentration (minor effect, correctable) |
| Cover by snow, ice, vegetation, soil, debris | Lower nuclide concentration (if unaccounted for, partly correctable) |

## 5.2 Interpretation of the Bleis Marscha boulder exposure ages

Our exposure ages in general anticorrelate with elevation and correlate with down-flow distance from the rock glacier root (Figs. 4, 7), conformable to the rock-glacier formation model. Nevertheless, ages from individual lobes show 'geologic scatter'. How do the processes listed in Table 4 apply to the Bleis Marscha rock glacier?

### 5.2.1 Boulder nuclide inventories on a moving rock glacier

505  Significant pre-exposure in the cirque headwalls seems unlikely because for talus rock glaciers like Bleis Marscha, fed by scree from the retreating headwall, headwall erosion is rapid (cf. Mohadjer et al., 2020; Steinemann et al., 2020). Back-of-the-envelope estimates of long-term average debris fluxes of the rock glacier lobe IV and V are in the order of 720 (<900) m$^3$ a$^{-1}$, calculated from mean speeds of 400 m/1200 a (length of lobe divided by exposure age), and a rock glacier width of 120 m (<150 m), a height of 30 m, and a debris fraction of 0.6. These debris fluxes correspond to head-wall erosion

510  rates of ~2.3–2.9 mm a$^{-1}$. At this accumulation rate meters of talus are built-up at the foot slope in decades to centuries as testified by the abundant fresh talus cones within the footprint of the LIA Bleis Marscha cirque glacier (Fig. 5a). With respect to their ice-cored moraine study, Crump et al. (2017) point out that it may be difficult to detect low levels of $^{10}$Be inheritance, but that it becomes unlikely for boulders larger than ca. 1 m side length because of strong self-shielding in the bedrock wall (rapid drop-off of $^{10}$Be production with depth). Boulders can also be exposed in the talus or any other reservoir

515  (e.g. moraine deposit) prior to entering the rock glacier system. Comparison of aerial photos over several years shows the rapid accumulation of talus since the LIA (see above), suggesting that nuclide accumulation in a boulder while in the talus or at the talus foot is likely not significant as the scree is quickly covered. Critically, the young exposure ages in unit V (see also below) verify rapid deposition onto the rock glacier. If inheritance from bedrock exposure is unlikely and storage in the talus with exposure at the surface is likely to be brief, then nuclide concentrations should record the time elapsed on the rock

520  glacier surface. This would include travel time and all of the time that a boulder is stable, whether in final relict deposit or when the rock glacier is less active. This suggests that most of the 'geologic scatter' of our data is due to post-depositional processes (Table 4), with instability in boulder position being the prime candidate.

Boulder GPS data reported by Lambiel and Delaloye (2004) demonstrate small (cm), slow, three-dimensional rotational movement of boulders, pointing to slightly variable orientation of the sampled surface and to the possibility of toppling or

525  overturning over longer periods of time. Boulders might roll or slide down steep scarps in front of rock glacier ridges (Kääb and Reichmuth, 2005) or topple into furrows. Ulrich et al. (2021) detected creep-independent, 'gravity-induced boulder movement' over a three week period at the steep (~30°) frontal part of the Äußeres Hochebenkar rock glacier with repeated terrestrial laser scans. Boulder instabilities are likely greater, the faster the rock glacier moves, and exacerbated by changes in surface elevation due to frost heave, thaw settlement, degradation or collapse of the underlying ice-rich core, similar to

530  ice-cored moraines (e.g. Crump et al., 2017), what we however did not observe on Bleis Marscha. Boulders are subangular to subrounded even in the youngest parts of the rock glacier (units IV–V; Fig. 6), evidence that knocking off of boulder corners during movement (jostling) or falling off the front of ridges is occurring. Addition of a boulder to a lobe due to recent rock fall as observed at Murtèl (Upper Engadine) in August 2020 (personal observation), would also yield a too young age. In the case of recent events, fresh boulder appearance calls this out. The effect of (~uniform) boulder surface weathering

535  is accounted for in the age calculation. It is only a few percent and lies within the uncertainties of an individual exposure age. On the other hand, (non-uniform) spalling, e.g. from frost shattering or friction between the boulders, potentially leads to

more severe lowering in nuclide concentration. Recently spalled surfaces, as revealed by their 'fresh' appearance, were not sampled. Unaccounted for shielding also leads to 'too young' exposure ages. The effect of snow cover was likely more pronounced for the smaller, less windswept boulders in the high-elevation lobes (units IV–V) where snow cover lasts longer, but also more uniform over the less rough surface. Strict constraints on how much snow and for how long hinder such a correction whose effect is limited to a few percent.

### 5.2.2 Three Bleis Marscha rock glacier generations

In light of the above discussion of the various factors contributing to cosmogenic nuclide concentrations in active rock glacier boulders, we now discuss the specific Bleis Marscha results. The cumulative effect of slight boulder instabilities and small under-exposure from rotation added up over millennia likely plays a role for the 'geologic scatter'. We think that the effect of stochastic boulder instabilities in general exceeds inheritance, although neither can be excluded in individual cases. The Bleis Marscha exposure ages are tendentially skewed towards 'too young'.

The morphologically continuous units I and II are the lower elevation, thus oldest units at Bleis Marscha. The exposure age of unit I is 8.9 ka (Err1, Fig. 6a). Of the three ages from boulders across unit II, two ages Err2 (7.0 ka) and Err15 (5.7 ka) are younger than the further up-slope boulder age Err14 at 8.1 ka (Fig. 6c, d). Boulders Err1 and Err14 are large and flat-lying with basal side lengths >3 m making it more likely that they roughly maintained their orientation as the rock glacier moved. In contrast, boulders Err2 and 15 are cigar-shaped, i.e. prone to rolling, and not very firmly embedded in the boulder mantle (Fig. 6b, c). We consider the ages for the latter two as 'too young'. We suggest that units I–II started forming at ~8.9 ka. Unit III occupies an intermediate topographic position in the Bleis Marsch rock glacier and is separated by a morphological discontinuity from the lower units I–II (Figs. 4, 5b). Two consistent ages Err13 (5.2 ka, Fig. 6d) and Err12 (4.8 ka, (Fig. 6e) also point to a 'time gap' between units I–II and unit III. The partly stabilized and vegetated terrain step immediately downstream of Err13 is the stabilized front of this lobe which we interpret to have formed at ~5.2–4.8 ka. Rock glacier units IV and V comprise the higher elevation more rapidly moving lobe of Bleis Marscha (Fig. 5a). Ages for unit IV range from 2.9 ka to 0.3 ka. The $^{36}$Cl age of 2.9 ka for Err8 seems incongruous with its position and the fact that a nearby boulder (Err9) is, at 0.7 ka $^{10}$Be age, 2 kyr younger. In comparison to the several dated boulders on unit IV, it is likely that boulder Err8 experienced pre-exposure in the bedrock. Inheritance is plausible given the small dimensions of the sampled boulder (0.7×1.0×1.5 m, Fig. 6g; see discussion above on Crump et al., 2017) and the crucial fact that $^{36}$Cl is produced deeper into rock than $^{10}$Be (Alfimov and Ivy-Ochs, 2009). This does not greatly affect our interpretation that lobe IV initiated at ~2.8 ka (age of Err11, Fig. 6f). The time gap to unit III coincides with a morphological (frontal terrain step) and kinematic discontinuity (Figs. 4, 8, 10b). Unit V is the highest elevation, youngest unit. It emanates from the footprint of the LIA glacier 100–150 m away from the foot of the talus, to what the two ages of 0.56 ka and 0.23 ka agree well.

We summarize the three interpreted Bleis Marscha formation phases, defined as the period during which the lobe is fed in the root zone (Fig. 11). Our data suggests that the early Holocene generation (units I–II) began forming at ~8.9 ka. The

formation phase lasted at least until ~8.1 ka as indicated by the upstream-most exposure age. Its youngest surface in the root zone has been overridden and buried by subsequent rock glacier generations. At the latest at ~5.2 ka, the minimum formation age of the mid-Holocene generation (unit III), units I–II must have been cut off from their debris source in the cirque. Analogously, the formation phase of the mid-Holocene generation with ages in the range ~5.2–4.8 ka ended at ~2.8 ka the latest, when it was overridden by unit IV and disconnected from the talus. The youngest late Holocene generation (units IV–V) began forming at ~2.8 ka. Coinciding morphological discontinuities (steep terrain steps, Fig. 4), 'time gaps', and kinematic discontinuities (velocity jumps, data gaps; Fig. 8) separate units I–II, III, and IV–V from each other. We interpret that Bleis Marscha is not a continuous 'stream', but a stack of three overriding lobes, each with its own, discrete formation phase.
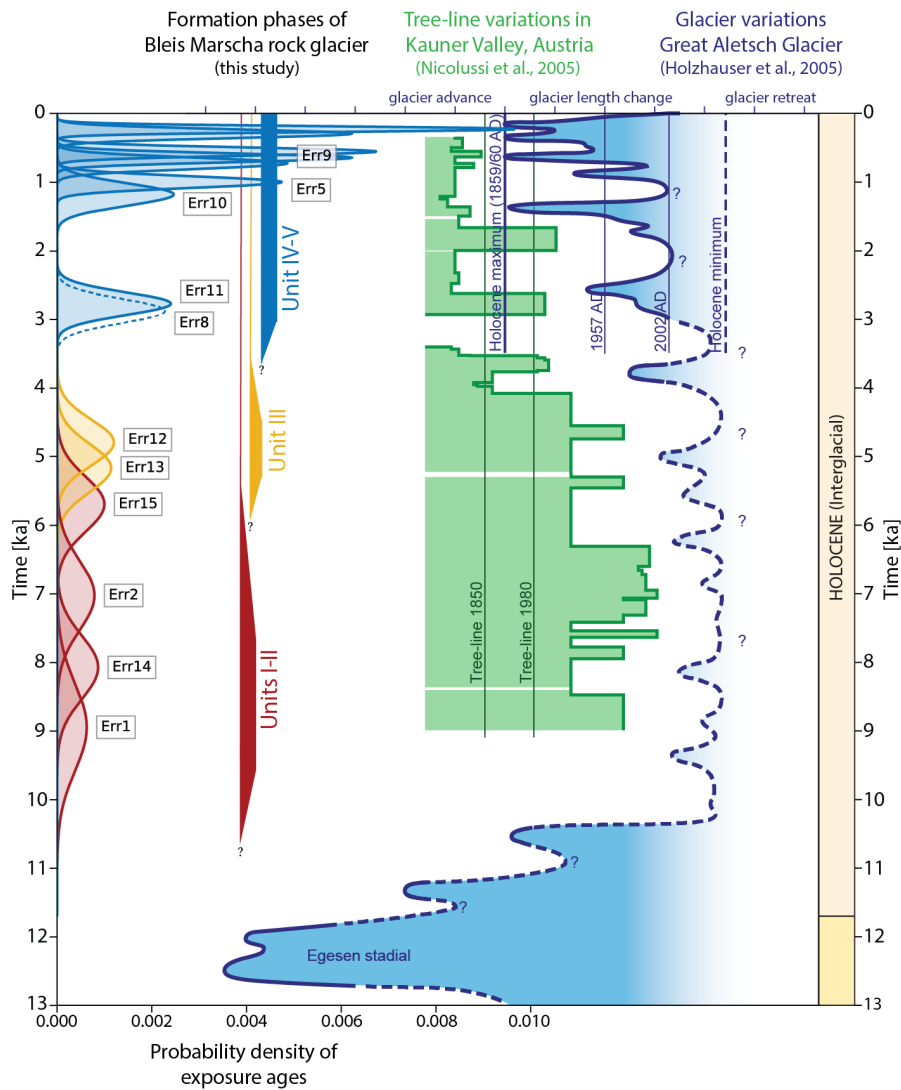
**Figure 11: Bleis Marscha rock glacier formation phases in the framework of the general climate evolution in the Central-Eastern Alps during the Younger Dryas and the Holocene (modified from Ivy-Ochs et al. (2009) and Singeisen et al. (2020)). Climate proxies are Great Aletsch glacier length variations (modified from Holzhauser et al., 2005) and Kauner valley tree-line variations (Nicolussi et al., 2005). We interpret three distinct generations: Early Holocene (~8.9–8.0 ka, after retreat of the Egesen glaciers of the Younger Dryas cold phase) of low-elevation units I–II, Middle Holocene (~5.2–4.8 ka, after thermal maximum) of unit III, and Late Holocene until present (since ~2.8 ka, roughly coeval with late Holocene cooling and glacier re-advances) of high-elevation units IV–V. The initiation of the three Bleis Marscha generations appear to correlate with Holocene climate oscillations.**

## 5.3 Implications

### 5.3.1 Episodic formation

In the Bleis Marscha cirque, Holocene rock glacier formation occurred in three distinct phases. These appear to be correlated to major Holocene climate shifts. The early Holocene generation (units I–II) is confined within, but not connected to Egesen lateral moraines (Schlosser, 1990). From this crosscutting relationship and the oldest and lowermost (minimum) formation age atop its front of 8.9 ka (Err1), it follows that these lobes must have formed after the Egesen cirque glacier starvation during the late Younger Dryas (Frauenfelder et al., 2001; Kerschner and Ivy-Ochs, 2008; Ivy-Ochs et al., 2009, Ivy-Ochs, 2015). After 10 ka, the climate shifted towards warmer conditions (Schimmelpfennig et al., 2014; Solomina et al., 2015). Already by the middle Holocene, the lower continuous permafrost boundary rose to likely above 2600 m a.s.l. (current -2°C MAAT isotherm, Fig. 3), and the tree line was higher than today (Fig. 11; Nicolussi et al., 2005). The early Holocene debris volume (units I–II) is twice the late Holocene debris volume (units IV–V) that took ~3 kyr to build up. This is a conservative estimate from the corresponding lengths (factor 1100 m/480 m ≈ 2.3) and surfaces areas (factor of ~2.7), assuming similar thickness and debris content, and that units I–II must extend as far up to their source of Err Granodiorite as both younger generations. Given the early Holocene warming and the formation timing of the mid-Holocene generation (~5.2–4.8 ka), it seems unlikely that the formation phase of the early Holocene generation was longer than 6 kyr. This rough comparison of debris supply rates points at a more intense early Holocene debris release compared to the late Holocene average. Possibly, the rapid early Holocene buildup was conditioned by debris from warming-induced rapid head wall weathering (Kenner and Magnusson, 2017; Kenner, 2018). Considering the climate resilience of debris-mantled Bleis Marscha lobes (discussed below), the end of the formation phase seems more likely linked to declining or imbalanced supply of debris and ice in proportions no longer susceptible for rock glacier creep.

The ages of the mid-Holocene unit III suggest a period of enhanced Bleis Marscha rock glacier activity at around 5 ka (~5.2–4.8 ka). Several lines of evidence, including radiocarbon data (Joerin et al., 2006) suggest a dominantly warm interval around that time perhaps punctuated by brief cold snaps (Solomina et al., 2015, 2016; Nicolussi et al., 2005, Kaufmann et al., 2020). Nevertheless, data from Tschingelgletscher (Berner Oberland; Wipf, 2001) and the Miage glacier (Mont Blanc massif, Deline and Orombelli, 2005) point to glacier advances around 5 ka, which is as well documented by the mummification of the Tyrolean Iceman after 5320–5050 cal BP (Kutschera et al., 2017) due to ice coverage which roughly persisted until 1991. Bohleber et al. (2020) point out an elevation dependency on the onset of middle to late Holocene glacier advances, suggesting that at the elevation of Bleis Marscha, the transition to colder conditions may have already begun.

In the late Holocene, after approximately 4 ka, climate cooled, timberline moved to lower elevations, and glacier advances became more frequent, longer and more severe compared to the middle Holocene, culminating in the LIA at ~1350–1850 CE (Fig. 11; Joerin et al., 2006; Ivy-Ochs et al., 2009; Le Roy et al., 2015; Solomina et al., 2016; Badino et al., 2018). Air temperature oscillations and concomitant freeze-thaw cycles weakened the headwall and increased frost shattering and debris

production, enhanced by the tectonically weakened fault zone in the headwall (Figs. 3–5a). Our data suggests that the late Holocene generation began forming roughly coeval with this climatic shift.

According to the dual-threshold model presented in Kirkbride and Brazier (1995), initiation of a new rock glacier lobe occurs when an external climate threshold and an internal talus thickness (shear-stress threshold) are crossed simultaneously. In Bleis Marscha cirque, debris production is high, as shown by the overfilled talus with lots of fresh rock fall since LIA (Fig. 5a). The internal threshold is not a limiting factor, and the Bleis Marscha rock glacier generations seem to reflect more the external climate threshold.

### 5.3.2 Slow degradation

The creep of the early-mid Holocene generations (units II–III), although with 15–35 cm a$^{-1}$ moving not as fast as the younger unit IV at 40–60 cm a$^{-1}$, is topographically controlled rather than by the creep susceptibility of the rock glacier body. This is shown by the good slope-creep rate correlation (Fig. 9) and the FE modelling results (Fig. 10). Moreover, cohesive creep and en bloc movement of these entire morphologically delineated lobes with sharp lateral velocity steps (Figs. 4, 7) indicates stress transmission and requires (excess) ice as 'cement' – notably beneath an early–middle Holocene boulder mantle, currently located below the -2°C MAAT isotherm (Fig. 2). Merely the southernmost fringe of the lowermost units I–II shows signs of incipient degradation. For lack of direct data on the interior of Bleis Marscha, the age of the inferred Bleis Marscha ice is not known and can principally be original or later recharged ice (Giardino and Vitek, 1988; Colucci et al., 2019). From the impression of a still intact looking microtopography (Fig. 5b), we think that the ice in units I–II and III is largely as old as its covering debris mantle, thus of early and mid-Holocene age, respectively. Otherwise, if advanced meltout occurred, the surface would look more disrupted and collapsed.

Persistence of ice is characteristic for rock glaciers, owed to the insulating openwork debris mantle (~active layer) and the cooling effect of air circulation (Colucci et al., 2019; Jones et al., 2019; Kellerer-Pirklbauer, 2019). For example, preservation of early Holocene ice through the mid-Holocene warm period is interpreted by Krainer et al. (2015) for the Lazaun rock glacier (South Tyrol). The close connection between surface substrate and ice preservation seems exemplified on Bleis Marscha by the stabilized right-lateral parts of unit III (Figs. 3, 5a), that do not move despite the mechanical load of the rapidly overriding unit IV. The local ground thermal regime beneath the fine-grained surface cover (fractured radiolarite) is less susceptible to permafrost conditions (Harris and Pedersen, 1998; Schneider et al., 2012).

### 5.3.3 Late Holocene glacier-rock glacier coexistence

During the late Holocene cold phases, the Bleis Marscha cirque was intermittently occupied at the most by a perennial ice patch or a glacieret (Frauenfelder et al, 2005), likely not larger than the LIA extent as mapped in the mid-19th century (Dufour, 1853; Siegfried, 1887). The thin, stagnant cirque glaciers could neither mechanically nor thermally erode the rock glacier; permafrost and the pre-existing rock glacier outlasted beneath the ice patches (Frauenfelder et al., 2001, 2005).

650 Stable cryotic conditions during the late Holocene are plausible in the high-elevation (>2700 m a.s.l.) cirque floor that is in the continuous permafrost belt even today (Gruber et al., 2006; Boeckli et al., 2012). "Mild" periods apparently were not long and warm enough for permafrost degradation, the more in view of the climate resilience of the debris-mantled ice-rich bodies. The equilibrium line altitude in the steep Bleis Marscha cirque headwalls oscillated in elevation, as likely did relative accumulation rates of ice and debris, with higher relative debris input during ice-free "mild" phases (Anderson et al., 2018; 655 Kenner et al., 2018). Also, the coarse debris transport alternated between glacial transport during cold phases and permafrost creep during glacial "mild" phases (Zasadni, 2005). Despite these oscillating growth conditions in the rock glacier root, the morphologically continuous surface (absent topographic steps) of unit IV with boulder exposure ages ranging from 0.5–2.8 ka suggests undisturbed growth from ~2.8 ka to pre-LIA.

## 6. Conclusions

660 We constrained formation phases and reconstructed the development of the active Bleis Marscha rock glacier (Val d'Err, eastern Switzerland) with morphostratigraphic relations from field observations, 15 cosmogenic nuclide exposure ages (14 $^{10}$Be and 1 $^{36}$Cl sample), modern (2003/2012) surface creep quantification from aerial image correlation, and finite element modelling to separate the control of topography and ice content on surface movement. In contrast to earlier works that exposure dated relict rock glaciers, the Bleis Marscha lobes are presently active. Boulder nuclide inventories are 665 stochastically overprinted primarily by the cumulative effect of small instabilities while travelling on the rock glacier surface. This leads to tendentially 'too young' exposure ages, although bedrock inheritance ('too old') cannot be excluded in individual cases. The correlation of two orthophotos from 2003 and 2012 indicates average movement at creep rates of 25–60 cm a$^{-1}$. Bleis Marscha is a 1100 m long, active, polymorphic talus rock glacier at an elevation range of 2400–2700 m a.s.l. Coinciding morphological discontinuities (terrain steps) and kinematic discontinuities (decorrelation gaps, velocity jumps) 670 separate the Bleis Marscha rock glacier in a stack of three lobes, each with its own formation phase. Our cosmogenic nuclide data suggest that the birth of each of the three lobes appears to correlate with Holocene climate shifts: Early Holocene, ~8.9–8.0 ka; Middle Holocene, ~5.2–4.8 ka; and Late Holocene, since ~2.8 ka.

Crosscutting relationships in the field indicate that the low-elevation, early Holocene generation of Bleis Marscha rock glacier formed after the retreat of the Egesen Bleis Marscha glacier, with exposure ages pointing at ~8.9–8.0 ka. The rapid 675 buildup of voluminous rock glacier bodies in the rapidly warming climate of the early Holocene was likely conditioned by warming-induced high rock-fall activity. The end of the formation phase could be linked to insufficient or imbalanced supply of debris and ice in proportions no longer susceptible for rock glacier creep. The mid-Holocene generation formed at ~5.2–4.8 ka during a dominantly warm period interrupted by short cold spells as documented by glacier advances. The formation phase of the high-elevation youngest late Holocene generation likely began at ~2.8 ka as indicated by its oldest exposure age 680 atop the front, roughly coeval with the onset of the late Holocene climate oscillations. Although these lobes are sourced in

the during late Holocene intermittently glacierized Bleis Marscha cirque, their morphological continuity suggests undisturbed growth. Due to favourable topo-climatic conditions in the high-elevation cirque (>2650 m a.s.l., MAAT -2°C) and small, stagnant cirque glacierets, ground thermal conditions in the rock glacier root zone remained cryotic and interactions with the glacieret were not disruptive for the rock glacier development. Ongoing cohesive surface deformation on old, early- and mid-Holocene Bleis Marscha lobes requires the presence of ice as stress transmitter. Although these lobes are below the current -2°C isotherm, we believe from the intact microtopography that the ice is largely original, preserved from the early/middle Holocene. Degradation of this azonal, ice-rich permafrost body, in contrast to its rapid formation, is slow and attenuated by the debris mantle. We find contrasting responses to external forcing of Bleis Marscha rock glacier parts: The successive initiation of three lobes in the Holocene suggests that rock glacier formation processes in the Bleis Marscha cirque were climate-sensitive, enabled by high rock-fall activity so that debris availability is not a limiting factor. Contrariwise, once formed, the boulder-mantled, ice-rich lobes reacted less sensitively to climate forcing, with permafrost degradation protracted over millennia.

*Author contributions.* S.I.-O., O.S., and M.F. designed the study. D.A., S.I.-O., O.S. and M.F. conducted the field work. O.S and D.A. carried out the [10]Be extraction, O.S. the [36]Cl extraction, and M.C. with C.V. the AMS measurements. D.A. computed the image correlation. D.A. and M.F. did the finite element modelling. D.A. prepared the figures and the manuscript which were edited by S.I.-O., O.S. and M.F.

*Acknowledgements.* We are grateful for the field support by Ueli Steinemann, Reto Grischott and Jonas von Wartburg. We thank Kristina Hippe and Ewelina Bros for their assistance during sample preparation and the Laboratory of Ion Beam Physics group for excellent AMS measurements. We thank Armando Janett (gamekeeper in municipality Surses), Carole Müller, and Peter Kaiser (Savognin) for their logistical support, and Reynald Delaloye (University of Fribourg) for the geomorphological discussions.

*Financial support.* D. Amschwand received financial support for the fieldwork by the Swiss Society for Quaternary Research. This work was completed in the framework of Swiss National Science Foundation project (SNF) 175794.

*Competing interests.* The authors declare that they have no conflict of interest.

# References

Alfimov, V. and Ivy-Ochs, S.: How well do we understand production of $^{36}$Cl in limestone and dolomite?, Quat Geochronol, 4, 462–474, https://doi.org/10.1016/j.quageo.2009.08.005, 2009.

Anderson, R. S., Anderson, L. S., Armstrong, W. H., Rossi, M. W., and Crump, S. E.: Glaciation of alpine valleys: The glacier – debris-covered glacier – rock glacier continuum, Geomorphology, 311, 127–142, https://doi.org/10.1016/j.geomorph.2018.03.015, 2018.

Arenson, L., Hoelzle, M., and Springman, S.: Borehole deformation measurements and internal structure of some rock glaciers in Switzerland, Permafrost Periglac, 13, 117–135, https://doi.org/10.1002/ppp.414, 2002.

Badino, F., Ravazzi, C., Vallè, F., Pini, R., Aceti, A., Brunetti, M., Champvillair, E., Maggi, V., Maspero, F., Perego, R., and Orombelli, G.: 8800 years of high-altitude vegetation and climate history at the Rutor Glacier forefield, Italian Alps. Evidence of middle Holocene timberline rise and glacier contraction, Quaternary Sci Rev, 185, 41–68, https://doi.org/10.1016/j.quascirev.2018.01.022, 2018.

Balco, G., Stone, J. O., Lifton, N. A., and Dunai, T. J.: A complete and easily accessible means of calculating surface exposure ages or erosion rates from $^{10}$Be and $^{26}$Al measurements, Quat Geochronol, 3, 174–195, https://doi.org/10.1016/j.quageo.2007.12.001, 2008.

Barsch, D.: Rockglaciers. Indicators for the Present and Former Geoecology in High Mountain Environments, Springer series in physical environment vol. 16, Springer, Berlin, Heidelberg, https://doi.org/10.1007/978-3-642-80093-1, 1996.

Bini, A., Buoncristiani, J.-F., Couterrand, S., Ellwanger, D., Felber, M., Florineth, D., Graf, H., Keller, O., Kelly, M., Schlüchter, C., and Schoeneich, P.: Die Schweiz während des letzteiszeitlichen Maximums (LGM) 1:500'000, Bundesamt für Landestopographie (swisstopo), Wabern, https://opendata.swiss/en/dataset/die-schweiz-wahrend-des-letzteiszeitlichen-maximums-lgm-1-500000, 2009.

Biot, M. A.: Theory of folding of stratified viscoelastic media and its implications in tectonics and orogenesis, GSA Bulletin, 72, 1595–1620, https://doi.org/10.1130/0016-7606(1961)72[1595:TOFOSV]2.0.CO;2, 1961.

Bodin, X., Krysiecki, J.-M., Schoeneich, P., Le Roux, O., Lorier, L., Echelard, T., Peyron, M., and Walpersdorf, A.: The 2006 collapse of the Bérard rock glacier (southern French Alps), Permafrost Periglac, 28, 209–223, https://doi.org/10.1002/ppp.1887, 2016.

Boeckli, L., Brenning, A., Gruber, S., and Noetzli, J.: Permafrost distribution in the European Alps: Calculation and evaluation of an index map and summary statistics (Alpine permafrost index map, APIM), The Cryosphere, 6, 807–820, https://doi.org/10.5194/tc-6-807-2012, 2012.

Bohleber, P., Schwikowski, M., Stocker-Waldhuber, M., Fang, L., and Fischer, A.: New glacier evidence for ice-free summits during the life of the Tyrolean Iceman, Sci Rep, 10, 20513, https://doi.org/10.1038/s41598-020-77518-9, 2020.

Böhlert, R., Compeer, M., Egli, M., Brandová, D., Maisch, M., W Kubik, P., and Haeberli, W.: A combination of relative-numerical dating methods indicates two high Alpine rock glacier activity phases after the glacier advance of the Younger Dryas, The Open Geography Journal, 4, 115–130, https://doi.org/10.2174/1874923201003010115, 2011a.

Böhlert, R., Egli, M., Maisch, M., Brandová, D., Ivy-Ochs, S., Kubik, P. W., and Haeberli, W.: Application of a combination of dating techniques to reconstruct the Lateglacial and early Holocene landscape history of the Albula region (eastern Switzerland), Geomorphology, 127, 1–13, https://doi.org/10.1016/j.geomorph.2010.10.034, 2011b.

Chandler, B. M. P., Lovell, H., Boston C. M., Lukas, S., Barr, I. D., Benediktsson, I. Ö., Benn, D. I., Clark, C. D., Darvill, C. M., Evans, D. J. A., Ewertowski, M. W., Loibl, D., Margold, M., Otto, J.-C., Roberts, D. H., Stokes, C. R., Storrar, R. D., and Stroeven, A. P.: Glacial geomorphological mapping: A review of approaches and frameworks for best practice, Earth-Sci Rev, 185, 806–846, https://doi.org/10.1016/j.earscirev.2018.07.015, 2018.

745 Christl, M., Vockenhuber, C., Kubik, P., Wacker, L., Lachner, J., Alfimov, V., and Synal, H.-A.: The ETH Zurich AMS facilities: Performance parameters and reference materials, Nuclear Instruments and Methods in Physics Research Section B: Beam Interactions with Materials and Atoms, 294, 29–38, https://doi.org/10.1016/j.nimb.2012.03.004, 2013.

Cicoira, A., Beutel, J., Faillettaz, J., and Vieli, A.: Water controls the seasonal rhythm of rock glacier flow, Earth Planet Sc Lett, 528, 115844, https://doi.org/10.1016/j.epsl.2019.115844, 2019.

750 Cicoira, A., Marcer, M., Gärtner-Roer, I., Bodin, X., Arenson, L., and Vieli, A.: A general theory of rock glacier creep based on in-situ and remote sensing observations, Permafrost Periglac, 1–15, https://doi.org/10.1002/ppp.2090, 2020.

Claude, A., Ivy-Ochs, S., Kober, F., Antognini, M., Salcher, B., and Kubik, P. W.: The Chironico landslide (Valle Leventina, southern Swiss Alps): Age and evolution, Swiss J Geosci, 107, 273–291, https://doi.org/10.1007/s00015-014-0170-z, 2014.

Colucci, R. R., Forte, E., Žebre, M., Maset, E., Zanettini, C., and Guglielmin, M.: Is that a relict rock glacier?, Geomorphology, 330, 177–189,
755 https://doi.org/10.1016/j.geomorph.2019.02.002, 2019.

Cornelius, H.P.: Geologische Karte der Err-Julier-Gruppe 1:25 000, 2 Blätter. Beitr. Geol. Karte Schweiz, Spezialkarte Nr. 115 A (Westblatt), 1932.

Crump, S. E., Miller, G. H., and Anderson, R. S.: Interpreting exposure ages from ice-cored moraines: a Neoglacial case study on Baffin Island, Arctic Canada, J Quaternary Sci, 32, 1049–1062, https://doi.org/10.1002/jqs.2979, 2017.

Debella-Gilo, M. and Kääb, A.: Locally adaptive template sizes for matching repeat images of Earth surface mass movements, ISPRS J Photogramm, 69,
760 10–28, https://doi.org/10.1016/j.isprsjprs.2012.02.002, 2012.

Degenhardt Jr., J. J. and Giardino, J. R.: Subsurface investigation of a rock glacier using ground-penetrating radar: Implications for locating stored water on Mars, J Geophys Res-Planet, 108, https://doi.org/10.1029/2002JE001888, 2003.

Delaloye, R., Lambiel, C., and Gärtner-Roer, I.: Overview of rock glacier kinematics research in the Swiss Alps, Geographica Helvetica, 65, 135–145, https://doi.org/10.5194/gh-65-135-2010, 2010.

765 Delaloye, R., Barboux, C., Bodin, X., Brenning, A., Hartl, L., Hu, Y., Ikeda, A., Kaufmann, V., Kellerer-Pirklbauer, A., Lambiel, C., Liu, L., Marcer, M., Rick, B., Scotti, R., Takadema, H., Trombotto Liaudat, D., Vivero, S., and Winterberger, M.: Rock glacier inventories and kinematics: A new IPA Action Group, in: Proceedings of the 5th European Conference on Permafrost, Chamonix-Mont Blanc, France, 23 June–1 July 2018, 392–393, 2018.

Deline, P. and Orombelli, G.: Glacier fluctuations in the western Alps during the Neoglacial, as indicated by the Miage morainic amphitheatre (Mont Blanc massif, Italy), Boreas, 34, 456–467, https://doi.org/10.1111/j.1502-3885.2005.tb01444.x, 2005.

770 Dufour, G.-H.: Topographische Karte der Schweiz, Blatt XV: Davos, Martinsbruck, Eidgenössische Landestopographie, Bern, 1853.

Fernández-Fernández, J. M., Palacios, D., Andrés, N., Schimmelpfennig, I., Tanarro, L. M., Brynjólfsson, S., López-Acevedo, F. J., Þorsteinn Sæmundsson, and A.S.T.E.R. Team: Constraints on the timing of debris-covered and rock glaciers: An exploratory case study in the Hólar area, northern Iceland, Geomorphology, 361, 107 196, https://doi.org/10.1016/j.geomorph.2020.107196, 2020.

Fitch, A. J., Kadyrov, A., Christmas, W. J., and Kittler, J.: Orientation correlation, in: Proceedings of the 13th British Machine Vision Conference, Cardiff,
775 United Kingdom, 2–5 September 2002, 133–142, http://citeseerx.ist.psu.edu/viewdoc/summary?doi=10.1.1.64.5662, 2002.

Frauenfelder, R. and Kääb, A.: Towards a palaeoclimatic model of rock-glacier formation in the Swiss Alps, Ann Glaciol, 31, 281–286, https://doi.org/10.3189/172756400781820264, 2000.

Frauenfelder, R., Haeberli,W., Hoelzle, M., and Maisch, M.: Using relict rockglaciers in GIS-based modelling to reconstruct Younger Dryas permafrost distribution patterns in the Err-Julier area, Swiss Alps, Norsk Geogr Tidsskr, 55, 195–202, https://doi.org/10.1080/00291950152746522, 2001.

780    Frauenfelder, R., Laustela, M., and Kääb, A.: Relative age dating of Alpine rockglacier surfaces, Z Geomorphol, NF, 49, 145–166, 2005.

Frehner, M., Ling, A. H. M., and Gärtner-Roer, I.: Furrow-and-ridge morphology on rockglaciers explained by gravity-driven buckle folding: A case study from the Murtèl rockglacier (Switzerland), Permafrost Periglac, 26, 57–66, https://doi.org/10.1002/ppp.1831, 2015.

Giardino, J. R. and Vitek, J. D.: The significance of rock glaciers in the glacial-periglacial landscape continuum, J Quaternary Sci, 3, 97–103, https://doi.org/10.1002/jqs.3390030111, 1988.

785    Gruber, S., Haeberli,W., Krummenacher, B., Keller, F., Mani, P., Hunziker, G., Hölzle, M., Vonder Mühll, D., Zimmermann, M., Keusen, H.-R., Götz, A., and Raetzo, H.: Erläuterungen zur Hinweiskarte der potentiellen Permafrostverbreitung in der Schweiz 1:50'000 (potential permafrost distribution map, PPDM), Bundesamt für Umwelt (BAFU), Bern, 2006.

Haeberli, W.: Creep of mountain permafrost: Internal structure and flow of Alpine rock glaciers, Mitteilungen der Versuchsanstalt für Wasserbau, Hydrologie und Glaziologie (VAW) an der ETH Zürich vol. 77, 1985.

790    Haeberli, W., Hoelzle, M., Kääb, A., Keller, F., Vonder Mühll, D., and Wagner, S.: Ten years after drilling through the permafrost of the active rock glacier Murtèl, Eastern Swiss Alps: Answered questions and new perspectives, in: Proceedings of the 7th International Conference on Permafrost, Yellowknife, Northwest Territories, Canada, 23–27 June 1998, 403–410, 1998.

Haeberli, W., Brandova, D., Burga, C., Egli, M., Frauenfelder, R., Kääb, A., Maisch, M., Mauz, B., and Dikau, R.: Methods for absolute and relative age dating of rock-glacier surfaces in Alpine permafrost, in: Proceedings of the 8th International Conference on Permafrost, Zürich, Switzerland, 21–25 July 795    2003, vol. 1, 343–348, 2003.

Haeberli, W., Hallet, B., Arenson, L., Elconin, R., Humlum, O., Kääb, A., Kaufmann, V., Ladanyi, B., Matsuoka, N., Springman, S., and Vonder Mühll, D.: Permafrost creep and rock glacier dynamics, Permafrost Periglac, 17, 189–214, https://doi.org/10.1002/ppp.561, 2006.

Haeberli, W., Schaub, Y., and Huggel, C.: Increasing risks related to landslides from degrading permafrost into new lakes in deglaciating mountain ranges, Geomorphology, 293, 405–417, https://doi.org/10.1016/j.geomorph.2016.02.009, 2017.

800    Hanson, S. and Hoelzle, M.: The thermal regime of the active layer at the Murtèl rock glacier based on data from 2002, Permafrost Periglac, 15, 273–282, https://doi.org/10.1002/ppp.499, 2004.

Harris, S. A. and Pedersen, D. E.: Thermal regimes beneath coarse blocky materials, Permafrost Periglac, 9, 107–120, https://doi.org/10.1002/(SICI)1099-1530(199804/06)9:2<107::AID-PPP277>3.0.CO;2-G, 1998.

Heyman, J., Stroeven, A. P., Harbor, J. M., and Caffee, M. W.: Too young or too old: Evaluating cosmogenic exposure dating based on an analysis of compiled boulder exposure ages, Earth Planet Sc Lett, 302, 71–80, https://doi.org/10.1016/j.epsl.2010.11.040, 2011. 805

Hock, R., Rasul, G., Adler, C., Cáceres, B., Gruber, S., Hirabayashi, Y., Jackson, M., Kääb, A., Kang, S., Kutuzov, S., ,Milner, Al., Molau, U., Morin, S., Orlove, B., and Steltzer, H.: High mountain areas, in: IPCC Special Report on the Ocean and Cryosphere in a Changing Climate, edited by: Pörtner, H.-O., Roberts, D.C., Masson-Delmotte, V., Zhai, P., Tignor, M., Poloczanska, E., Mintenbeck, K., Alegría, A., Nicolai, M., Okem, A., Petzold, J., Rama, B., Weyer, N.M., 131–202, 2019.

810    Holzhauser, H., Magny, M., and Zumbühl, H. J.: Glacier and lake-level variations in west-central Europe over the last 3500 years, The Holocene, 15, 789–801, https://doi.org/10.1191/0959683605hl853ra, 2005.

Humlum, O.: The climatic significance of rock glaciers, Permafrost Periglac, 9, 375–395, https://doi.org/10.1002/(SICI)1099-1530(199810/12)9:4<375::AID-PPP301>3.0.CO;2-0, 1998.

Ivy-Ochs, S.: Glacier variations in the European Alps at the end of the last glaciation, Cuadernos de Investigación Geográfica, 41, 295–315, https://doi.org/10.18172/cig.2750, 2015.

Ivy-Ochs, S., Kerschner, H., and Schlüchter, C.: Cosmogenic nuclides and the dating of Lateglacial and Early Holocene glacier variations: the Alpine perspective. Quatern Int, 164, 53–63, https://doi.org/10.1016/j.quaint.2006.12.008, 2007.

Ivy-Ochs, S. and Kober, F.: Surface exposure dating with cosmogenic nuclides, Quaternary Science Journal, 57, 179–209, https://www.eg-quaternary-sci-j.net/57/179/2008/, 2008.

Ivy-Ochs, S., Synal, H.-A., Roth, C., and Schaller, M.: Initial results from isotope dilution for Cl and $^{36}$Cl measurements at the PSI/ETH Zurich AMS facility, Nuclear Instruments and Methods in Physics Research Section B: Beam Interactions with Materials and Atoms, 223-224, 623–627, https://doi.org/10.1016/j.nimb.2004.04.115, 2004.

Ivy-Ochs, S., Kerschner, H., Maisch, M., Christl, M., Kubik, P. W., and Schlüchter, C.: Latest Pleistocene and Holocene glacier variations in the European Alps, Quaternary Sci Rev, 28, 2137–2149, https://doi.org/10.1016/j.quascirev.2009.03.009, 2009.

Joerin, U. E., Stocker, T. F., and Schlüchter, C.: Multicentury glacier fluctuations in the Swiss Alps during the Holocene, The Holocene, 16, 697–704, https://doi.org/10.1191/0959683606hl964rp, 2006.

Jones, D. B., Harrison, S., Anderson, K., and Whalley, W. B.: Rock glaciers and mountain hydrology: A review, Earth-Sci Rev, 193, 66–90, https://doi.org/10.1016/j.earscirev.2019.04.001, 2019.

Kääb, A. and Reichmuth, T.: Advance mechanisms of rock glaciers, Permafrost Periglac, 16, 187–193, http://dx.doi.org/10.1002/ppp.507, 2005.

Kääb, A., Haeberli, W., and Gudmundsson, G. H.: Analysing the creep of mountain permafrost using high precision aerial photogrammetry: 25 years of monitoring Gruben rock glacier, Swiss Alps, Permafrost Periglac, 8, 409–426, https://doi.org/10.1002/(SICI)1099-1530(199710/12)8:4<409::AID-PPP267>3.0.CO;2-C, 1997.

Kaufman, D., McKay, N., Routson, C., Erb, E., Dätwyler, C., Sommer, P. S., Heiri, O., and Davis, B.: Holocene global mean surface temperature, a multi-method reconstruction approach, Sci Data, 7, https://doi.org/10.1038/s41597-020-0530-7, 2020.

Kellerer-Pirklbauer, A.: Long-term monitoring of sporadic permafrost at the eastern margin of the European Alps (Hochreichart, Seckauer Tauern range, Austria), Permafrost Periglac, 30, 260–277, https://doi.org/10.1002/ppp.2021, 2019.

Kenner, R.: Geomorphological analysis on the interaction of Alpine glaciers and rock glaciers since the Little Ice Age, Land Degrad Dev, 30, 580–591, https://doi.org/10.1002/ldr.3238, 2018.

Kenner, R. and Magnusson, J.: Estimating the effect of different influencing factors on rock glacier development in two regions in the Swiss Alps, Permafrost Periglac, 28, 195–208, https://doi.org/10.1002/ppp.1910, 2017.

Kenner, R., Bühler, Y., Delaloye, R., Ginzler, C., and Phillips, M.: Monitoring of high Alpine mass movements combining laser scanning with digital airborne photogrammetry, Geomorphology, 206, 492–504, https://doi.org/10.1016/j.geomorph.2013.10.020, 2014.

Kenner, R.; Noetzli, J.; Hoelzle, M.; Raetzo, H. and Phillips, M.: Distinguishing ice-rich and ice-poor permafrost to map ground temperatures and ground ice occurrence in the Swiss Alps, The Cryosphere, 13, 1925–1941, https://doi.org/10.5194/tc-13-1925-2019, 2019

Kerschner, H. and Ivy-Ochs, S.: Palaeoclimate from glaciers: Examples from the Eastern Alps during the Alpine Lateglacial and early Holocene, Global Planet Change, 60, 58–71, https://doi.org/10.1016/j.gloplacha.2006.07.034, 2008.

Kirkbride, M. and Brazier, V.: On the sensitivity of Holocene talus-derived rock glaciers to climate change in the Ben Ohau Range, New Zealand, J Quaternary Sci, 10, 353–365, https://doi.org/10.1002/jqs.3390100405, 1995.

Knight, J., Harrison, S., and Jones, D. B.: Rock glaciers and the geomorphological evolution of deglacierizing mountains, Geomorphology, 324, 14–24, https://doi.org/10.1016/j.geomorph.2018.09.020, 2019.

Krainer, K., Bressan, D., Dietre, B., Haas, J. N., Hajdas, I., Lang, K., Mair, V., Nickus, U., Reidl, D., Thies, H., and Tonidandel, D.: A 10,300-year-old permafrost core from the active rock glacier Lazaun, southern Ötztal Alps (South Tyrol, northern Italy), Quaternary Res, 83, 324–335, https://doi.org/10.1016/j.yqres.2014.12.005, 2015.

Kronig, O., Ivy-Ochs, S., Hajdas, I., Christl, M., Wirsig, C., and Schlüchter, C.: Holocene evolution of the Triftje- and the Oberseegletscher (Swiss Alps) constrained with [10]Be exposure and radiocarbon dating, Swiss J Geosci, https://doi.org/10.1007/s00015-017-0288-x, 2018.

Kutschera, W., Patzelt, G., Steier, P., and Wild, E.: The Tyrolean Iceman and his glacial environment during the Holocene, Radiocarbon, 59, 395–405. https://doi.org/10.1017/RDC.2016.70, 2017.

Lal, D.: Cosmic ray labeling of erosion surfaces: in situ nuclide production rates and erosion models, Earth Planet Sc Lett, 104, 424–439, https://doi.org/10.1016/0012-821X(91)90220-C, 1991.

Lambiel, C. and Delaloye, R.: Contribution of real-time kinematic GPS in the study of creeping mountain permafrost: examples from the Western Swiss Alps. Permafrost Periglac, 15, 229–241, https://doi.org/10.1002/ppp.496, 2004.

Laustela, M., Egli, M., Frauenfelder, R., Kääb, A., Maisch, M., and Haeberli, W.: Weathering rind measurements and relative age dating of rockglacier surfaces in crystalline regions of the Eastern Swiss Alps, in: Proceedings of the 8th International Conference on Permafrost, Zürich, Switzerland, 21–25 July 2003, 627–632, 2003.

Le Roy, M., Nicolussi, K., Deline, P., Astrade, L., Edouard, J.-L., Miramont, C., and Arnaud, F.: Calendar-dated glacier variations in the western European Alps during the Neoglacial: the Mer de Glace record, Mont Blanc massif, Quaternary Sci Rev, 108, 1–22, https://doi.org/10.1016/j.quascirev.2014.10.033, 2015.

Marcer, M., Serrano, C., Brenning, A., Bodin, X., Goetz, J., and Schoeneich, P.: Evaluating the destabilization susceptibility of active rock glaciers in the French Alps, The Cryosphere, 13, 141–155, https://doi.org/10.5194/tc-13-141-2019, 2019.

Messerli, A. and Grinsted, A.: Image georectification and feature tracking toolbox: ImGRAFT, Geosci Instrum Meth, 4, 23–34, https://doi.org/10.5194/gi-4-23-2015, 2015.

Mohadjer, S., Ehlers, T.A., Nettesheim, M, Ott, M.B., Glotzbach, C., and Drews, R.: Temporal variations in rockfall and rock-wall retreat rates in a deglaciated valley over the past 11 k.y., Geology, 48, 594–598, https://doi.org/10.1130/G47092.1, 2020.

Moore, P. L.: Deformation of debris-ice mixtures, Rev Geophys, 52, 435–467, https://doi.org/10.1002/2014RG000453, 2014.

Moran, A. P., Ivy-Ochs, S., Vockenhuber, C., and Kerschner, H.: Rock glacier development in the Northern Calcareous Alps at the Pleistocene-Holocene boundary, Geomorphology, 273, 178–188, https://doi.org/10.1016/j.geomorph.2016.08.017, 2016.

Müller, J., Vieli, A., and Gärtner-Roer, I.: Rock glaciers on the run – understanding rock glacier landform evolution and recent changes from numerical flow modeling, The Cryosphere, 10, 2865–2886, https://doi.org/10.5194/tc-10-2865-2016, 2016.

Nicolussi, K., Kaufmann, M., Patzelt, G., Thurner, A., van der Plicht, J., and Thurner, A.: Holocene tree-line variability in the Kauner Valley, Central Eastern Alps, indicated by dendrochronological analysis of living trees and subfossil logs, Veg Hist Archaeobot, 14, 221–234, https://doi.org/10.1007/s00334-005-0013-y, 2005.

Noetzli, J., Pellet, C., and Staub, B. (Eds.): PERMOS 2019. Permafrost in Switzerland 2014/2015 to 2017/2018., Glaciological Report (Permafrost) No. 16–19 of the Cryospheric Commission of the Swiss Academy of Sciences, 104 pp., https://doi.org/10.13093/permos-rep-2019-16-19, 2019.

Nye, J. F.: The Mechanics of Glacier Flow, J Glaciol, 2, 82–93, https://doi.org/10.3189/S0022143000033967, 1952.

885 Scapozza, C., Lambiel, C., Bozzini, C., Mari, S., and Conedera, M.: Assessing the rock glacier kinematics on three different timescales: A case study from the southern Swiss Alps, Earth Surf Proc Land, 39, 2056–2069, https://doi.org/10.1002/esp.3599, 2014.

Schimmelpfennig, I., Schaefer, J. M., Akçar, N., Koffman, T., Ivy-Ochs, S., Schwartz, R., Finkel, R. C., Zimmerman, S., and Schlüchter, C.: A chronology of Holocene and Little Ice Age glacier culminations of the Steingletscher, Central Alps, Switzerland, based on high sensitivity beryllium-10 moraine dating, Earth Planet Sc Lett, 393, 220–230, https://doi.org/10.1016/j.epsl.2014.02.046, 2014.

890 Schlosser, O.: Geomorphologische Kartierung und glazialmorphologische Untersuchungen in der Err-Gruppe (Oberhalbstein, Kt. Graubünden), unpublished diploma thesis, Dept. of Geography, University of Zurich, 90 pp., 1990.

Schneider, S., Hoelzle, M., and Hauck, C.: Influence of surface and subsurface heterogeneity on observed borehole temperatures at a mountain permafrost site in the Upper Engadine, Swiss Alps, The Cryosphere, 6, 517–531, https://doi.org/10.5194/tc-6-517-2012, 2012.

Schwanghart, W. and Scherler, D.: Short Communication: TopoToolbox 2 – MATLAB-based software for topographic analysis and modelling in Earth
895 surface sciences, Earth Surf Dynam, 2, 1–7, https://doi.org/10.5194/esurf-2-1-2014, 2014.

Scotti, R., Crosta, G. B., and Villa, A.: Destabilisation of creeping permafrost: The Plator rock glacier case study (central Italian Alps), Permafrost Periglac, 28, 224–236, https://doi.org/10.1002/ppp.1917, 2017.

Shewchuk, J. R.: Triangle: Engineering a 2D quality mesh generator and Delaunay triangulator, pp. 203–222, Springer, Berlin, Heidelberg, https://doi.org/10.1007/BFb0014497, 1996.

900 Siegfried, H.: Topographischer Atlas der Schweiz 1:25 000/1:50 000, Blatt 426: Savognin, Eidgenössische Landesopographie, Bern, 1887.

Singeisen, C., Ivy-Ochs, S., Wolter, A., Steinemann, O., Akçar, N., Yesilyurt, S., and Vockenhuber, C.: The Kandersteg rock avalanche (Switzerland): Integrated analysis of a late Holocene catastrophic event, Landslides, 17, 1297–1317, https://doi.org/10.1007/s10346-020-01365-y, 2020.

Solomina, O. N., Bradley, R. S., Hodgson, D. A., Ivy-Ochs, S., Jomelli, V., Mackintosh, A. N., Nesje, A., Owen, L. A., Wanner, H., Wiles, G. C., and Young, N. E.: Holocene glacier fluctuations, Quaternary Sci Rev, 111, 9–34, https://doi.org/10.1016/j.quascirev.2014.11.018, 2015.

905 Solomina, O. N., Bradley, R. S., Jomelli, V., Geirsdottir, A., Kaufman, D. S., Koch, J., McKay, N. P., Masiokas, M., Miller, G., Nesje, A., Nicolussi, K., Owen, L. A., Putnam, A. E., Wanner, H., Wiles, G., and Yang, B.: Glacier fluctuations during the past 2000 years, Quaternary Sci Rev, 149, 61–90, https://doi.org/10.1016/j.quascirev.2016.04.008, 2016.

Sorg, A., Kääb, A., Roesch, A., Bigler, C., and Stoffel, M.: Contrasting responses of Central Asian rock glaciers to global warming, Scientific reports, 5, 8228, https://doi.org/10.1038/srep08228, 2015.

910 Springman, S. M., Arenson, L. U., Yamamoto, Y., Maurer, H., Kos, A., Buchli, T., and Derungs, G.: Multidisciplinary investigations on three rock glaciers in the Swiss Alps: Legacies and future perspectives, Geogr Ann A, 94, 215–243, https://doi.org/10.1111/j.1468-0459.2012.00464.x, 2012.

Steinemann, O., Reitner, J. M., Ivy-Ochs, S., Christl, M., and Synal, H.-A.: Tracking rockglacier activity in the Eastern Alps from the Lateglacial to the early Holocene, Quat Sci Rev, 241, https://doi.org/10.1016/j.quascirev.2020.106424, 2020.

Stone, J. O.: Air pressure and cosmogenic isotope production, J Geophys Res-Sol Ea, 105, 23 753–23 759, https://doi.org/10.1029/2000JB900181, 2000.

915 Synal, H.-A., Bonani, G., Döbeli, M., Ender, R., Gartenmann, P., Kubik, P., Schnabel, C., and Suter, M.: Status report of the PSI/ETH AMS facility, Nuclear Instruments and Methods in Physics Research Section B: Beam Interactions with Materials and Atoms, 123, 62–68, https://doi.org/10.1016/S0168-583X(96)00608-8, 1997.

Ulrich, V., Williams, J. G., Zahs, V., Anders, K., Hecht, S., and Höfle, B.: Measurement of rock glacier surface change over different timescales using terrestrial laser scanning point clouds, Earth Surf Dynam, 9, 19–28, https://doi.org/10.5194/esurf-9-19-2021, 2021.

920 Vockenhuber, C., Miltenberger, K.-U., and Synal, H.-A.: [36]Cl measurements with a gas-filled magnet at 6 MV, Nuclear Instruments and Methods in Physics Research Section B: Beam Interactions with Materials and Atoms, 455, 190–194, https://doi.org/10.1016/j.nimb.2018.12.046, 2019.

Wicky, J. and Hauck, C.: Numerical modelling of convective heat transport by air flow in permafrost talus slopes, The Cryosphere, 11, 1311–1325, https://doi.org/10.5194/tc-11-1311-2017, 2017.

Winkler, S. and Lambiel, C.: Age constraints of rock glaciers in the Southern Alps/New Zealand – Exploring their palaeoclimatic potential, The Holocene, 925 28, 778–790, https://doi.org/10.1177/0959683618756802, 2018.

Wipf, A.: Gletschergeschichtliche Untersuchungen im spät- und postglazialen Bereich des Hinteren Lauterbrunnentals (Berner Oberland, Schweiz), Geogr. Helv., 56, 133–144, https://doi.org/10.5194/gh-56-133-2001, 2001.

Wirz, V., Gruber, S., Purves, R. S., Beutel, J., Gärtner-Roer, I., Gubler, S., and Vieli, A.: Short-term velocity variations at three rock glaciers and their relationship with meteorological conditions, Earth Surf Dynam, 4, 103–123, https://doi.org/10.5194/esurf-4-103-2016, 2016.

930 Zasadni, J.: The Little Ice Age in the Alps: Its record in glacial deposits and rock glacier formation, Studia Geomorphologica Carpatho-Balcanica, 41, 117–137, 2007.